communications earth & environment

Article

https://doi.org/10.1038/s43247-024-01958-8

Strong El Niño and La Niña precipitation—sea surface temperature sensitivity under a carbon removal scenario

Check for updates

Chao Liu [1], Soon-Il An [1,2] ✉, Zixiang Yan[3,4], Soong-Ki Kim [1] & Seungmok Paik [1]

El Niño-Southern Oscillation-induced tropical Pacific precipitation anomalies have global impacts and will intensify under greenhouse warming, but the potential for mitigating these changes is less understood. Here, we identify distinct hysteresis features in the precipitation-sea surface temperature sensitivity between strong El Niño and La Niña phases using a large ensemble carbon removal numerical simulation. The strong El Niño precipitation sensitivity exhibits a century-scale hysteretic enhancement and eastward shift, mainly due to modulated deep convection anomalies by the Intertropical Convergence Zone via cloud-longwave feedback. Instead, the strong La Niña counterpart is concentrated toward the equator, mostly in the central-western Pacific, with a shorter hysteresis period of a few decades. This primarily involves changes in shallow convection and surface thermal structures during La Niña, shaped by global warming-induced upper-ocean circulation changes. The distinct climate change regimes of strong El Niño and La Niña precipitation sensitivity hold important implications for assessing mitigation consequences.

The El Niño–Southern Oscillation (ENSO) is the strongest interannual variability with widespread socioeconomic impacts[1–4]. In particular, ENSO-induced precipitation anomalies in the tropical central-eastern Pacific and the associated diabatic heating strongly determine the local atmospheric responses, which not only feed back into the initial ENSO sea surface temperature (SST) perturbations via multiple ocean-atmosphere feedback processes, but also influence the ENSO atmospheric teleconnection by shaping upper-level Rossby wave sources[5,6]. Thus, ENSO precipitation is important for both ENSO dynamics and remote impacts, and a better understanding of its future changes can help reduce uncertainties in ENSO characteristics and teleconnection projections[7–9].

The response of ENSO precipitation to anthropogenic warming has been extensively studied over the past decade[10–18]. Most climate models suggest that future ENSO precipitation will intensify and move eastward with an El Niño-like mean state warming[17,19]. The underlying physical causes are generally twofold, involving a thermodynamic contribution from increased background moisture and a dynamical contribution from enhanced ENSO-induced anomalous upward motions[12]. The former, constrained by the Clausius-Clapeyron relation (saturation vapor pressure increases by about 7% for each 1 K rise in temperature)[20], is linear and qualitatively robust across models, while the latter, largely related to ENSO SST intensity and structure[12–14,17], has a higher degree of model dependence, as most current models still struggle to realistically represent ENSO ocean-atmosphere coupled dynamics and provide credible future changes[21,22].

Although the moisture analysis is intuitive for understanding ENSO precipitation, the ultimate causes of ENSO-scale upward motions and their modulation by background conditions cannot be readily answered within the moisture framework. Previous studies have suggested two main types of vertical motion profiles over the tropical ocean with distinct destabilization mechanisms by the underlying SST[23,24], including the top-heavy structure (deep convection) in the western Pacific and the bottom-heavy structure (shallow convection) prevailing in the eastern Pacific Intertropical Convergence Zone (ITCZ) region[25]. Deep convection is largely controlled by the gross moist stability, the moist static energy (MSE) difference between the upper and surface levels[26]. For example, a warm SST anomaly typically reduces gross moist stability, facilitating anomalous upward motion and deep convective precipitation. Under global warming, El Niño-like background warming destabilizes the background atmospheric environment, allowing the same SST perturbation to trigger stronger anomalous upward motions[27]. In contrast, shallow convection relies more on boundary layer processes, where the spatial distribution of the SST anomaly shapes the surface pressure, which in turn drives surface winds, moisture convergence,

[1]Irreversible Climate Change Research Center (IRCC), Yonsei University, Seoul, Republic of Korea. [2]Department of Atmospheric Sciences, Yonsei University, Seoul, Republic of Korea. [3]Shanghai Investigation, Design and Research Institute Co., Ltd, Shanghai, China. [4]Key Laboratory of Polar Atmosphere-Ocean-Ice System for Weather and Climate of the MOE, Department of Atmospheric and Oceanic Science & Institute of Atmospheric Science, Fudan University, Shanghai, China. ✉e-mail: sian@yonsei.ac.kr

and precipitation anomalies[23,28,29]. Therefore, mean state modulated changes in the ENSO SST structure also contribute to ENSO precipitation changes. For example, a recent study[17] based on the HadCM3C model suggests that the shallow convection changes due to a meridionally narrowed ENSO SST may hold the key to ENSO precipitation intensification and eastward shift in a warming climate.

In addition to the global warming scenario, recent studies[30,31] using a large ensemble simulation of the Community Earth System Model Version 1.2 (CESM1.2) have found that ENSO characteristics under a reversed CO_2 removal scenario exhibit prominent hysteresis features relative to the CO_2 forcing. For example, the frequency of convective extreme El Niño events shows a stronger increase during the CO_2 ramp-down phase than during the ramp-up phase[32], which is likely related to the tropical Pacific ITCZ hysteresis[33]. Similar hysteresis, mainly associated with strong ENSO events, is also seen in ENSO SST[30,31] and teleconnections[34], and is more pronounced in the El Niño phase than in the La Niña phase[31], suggesting distinct background modulation processes behind.

So far, the overall response of ENSO precipitation to CO_2 removal has not been systematically studied, and the associated mean state modulating processes remain less clear, motivating us to further understand this issue. Our simulation is suitable for this topic for the following reasons: (i) the CESM1.2 model has reasonable performance in capturing the basic dynamics and complexity features of ENSO, and has been widely used to study ENSO responses under different climate change conditions[35–40]; (ii) the CO_2 ramp-up and ramp-down experiment involves time-varying changes in background conditions compared to the unidirectional changes in global warming scenarios, and allows the study of mean state-dependent ENSO responses; (iii) 28 large ensemble members allow good separation of forced changes from internal variability. To minimize the influence of SST variability changes, we here focused on changes in strong ENSO precipitation-SST sensitivity and their physical causes using a precipitation analysis framework that considers different types of convection[17,27,41]. We found distinct precipitation-SST sensitivity responses between strong El Niño and La Niña to decarbonization, driven by different ocean-atmosphere mean state forcers.

Results

Changes in strong ENSO precipitation-SST sensitivity

The ENSO precipitation-SST sensitivity, the response of tropical Pacific precipitation anomaly to a unit ENSO SST perturbation during ENSO peak phase (December to February, DJF), is calculated using a phase-dependent regression analysis (Methods) with an ENSO SST index over the main action center (180°-90°W, 5°S-5°N). Similar analyses are applied to other ENSO-related quantities, including SST, atmospheric circulation, and feedback processes. The regression result is more representative of strong ENSO events[42], which drive most ENSO variability (Supplementary Fig. 1) and exhibit pronounced hysteresis changes[30–32]. In the CESM1.2 present-day (PD) simulation ("Methods"), strong El Niño SST warming is accompanied by basin-scale positive precipitation anomalies (Supplementary Fig. 2e), whereas during the La Niña phase, basin-scale SST anomalies induce strong precipitation mainly at its margin in the central-western Pacific (Supplementary Fig. 2m). The horizontal distribution and equatorial vertical profile of the key moisture feedback process (i.e., moisture advection by anomalous vertical motions) and associated physical quantities are generally similar to the observations (Supplementary Figs. 2, 3), suggesting an overall reasonable model performance. Note that our model follows some common model biases in ENSO atmospheric responses[43–45], including a slightly weaker precipitation sensitivity, with patterns that extend farther

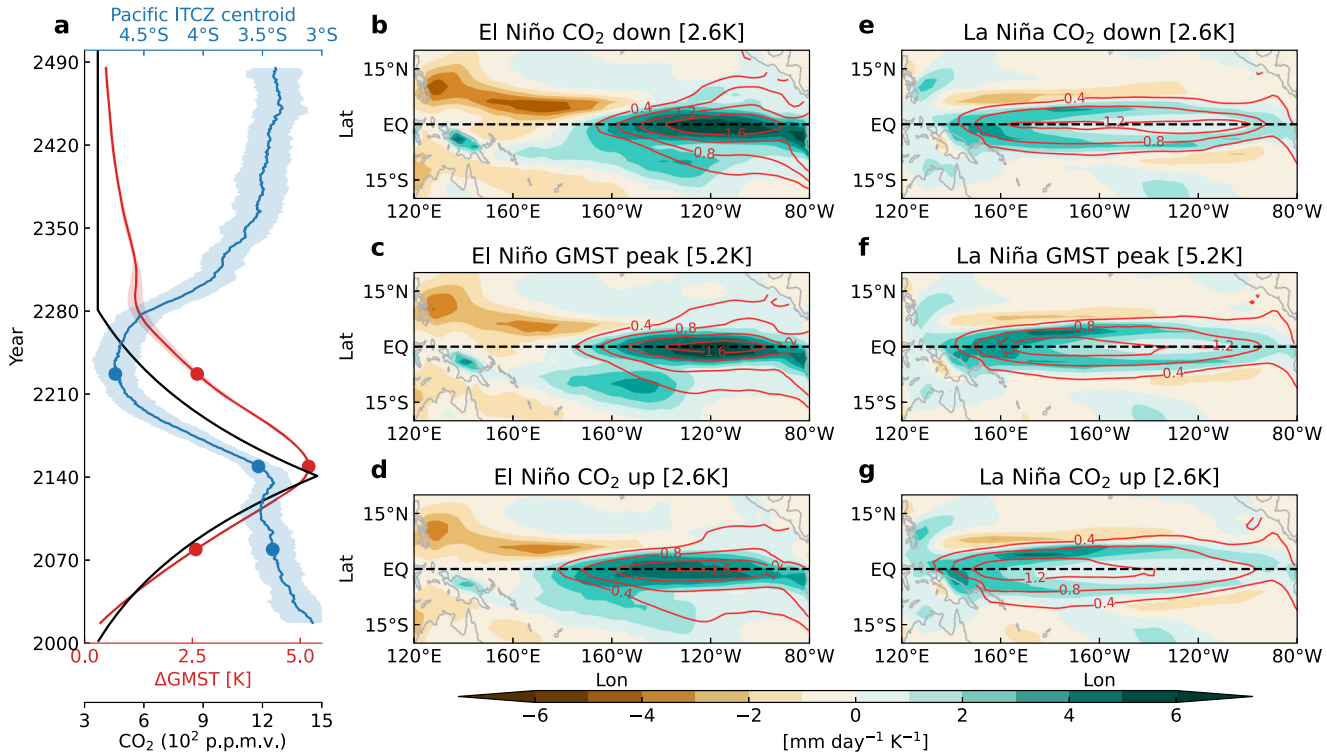


Fig. 1 | Changes in strong El Niño and La Niña precipitation sensitivity and background forcers. a Time evolution of CO_2 concentration (black, unit: ppmv), changes in ensemble-averaged global mean surface temperature (GMST; red, unit: K), and centroid of zonal mean precipitation (blue, unit: degrees latitude) in the tropical Pacific (120°E-80°W, 20°S-20°N) during the DJF season in the CESM1.2 model. Shading represents the range of two standard deviations among 28 ensemble members. The ITCZ centroid is defined as the latitude that equally divides the DJF tropical Pacific zonal mean precipitation. **b–d** Ensemble-averaged horizontal maps of regressed El Niño precipitation (shading, unit: mm day^{-1} K^{-1}) and SST (contours, unit: K K^{-1}) anomalies during the DJF season on the concurrent ENSO SST index (90°–180°W, 5°S–5°N) in a 31-year window centered on the CO_2 increase (2079), GMST peak (2149), and CO_2 decrease (2227) phases. The timing of three selected slices is based on GMST and are indicated by markers in (**a**). **e–g** as **b–d**, but for the La Niña phase. The Δ symbol indicates the ensemble-average change relative to the control simulation ensemble average.

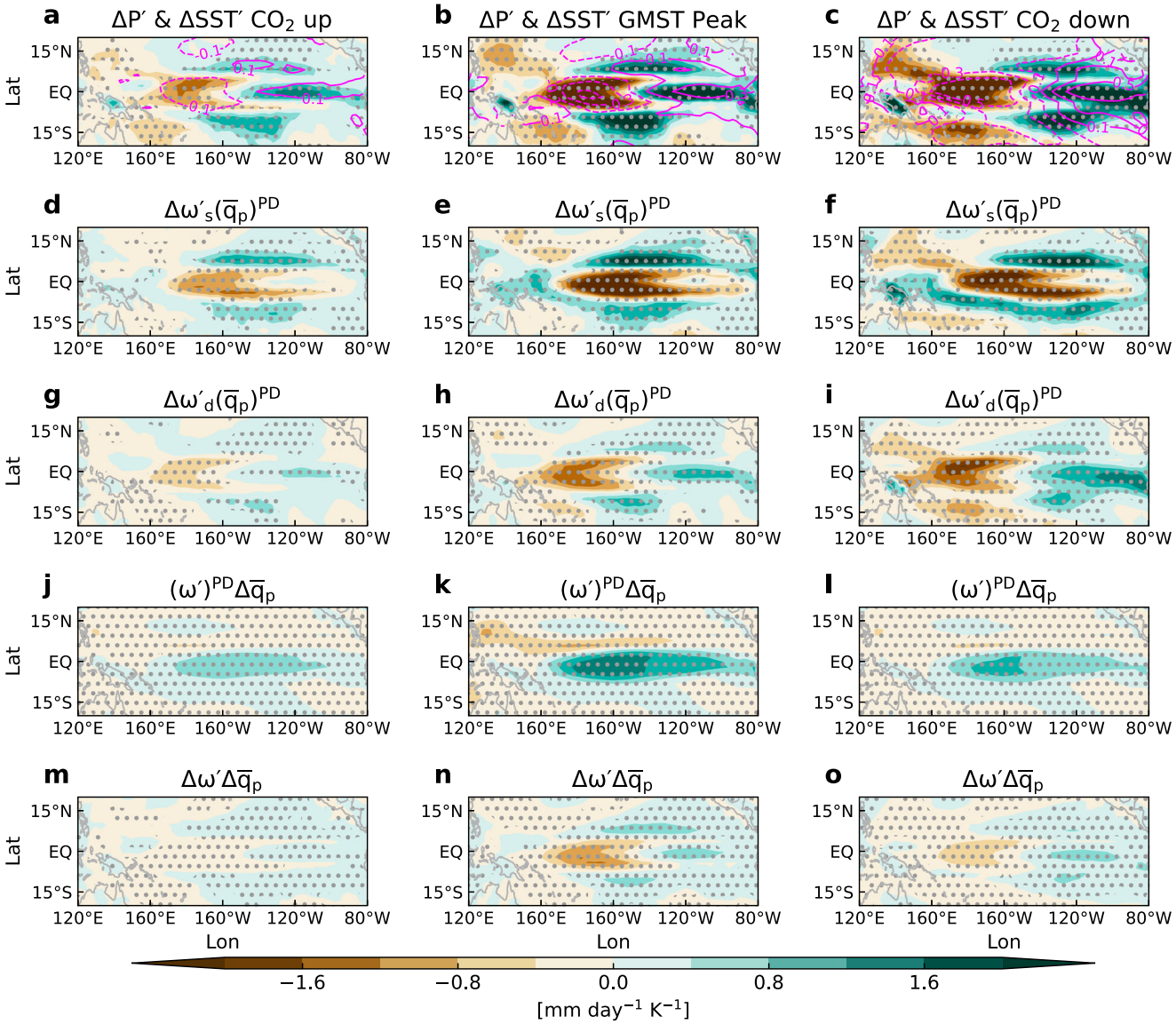


Fig. 2 | El Niño moisture budget. a–c Horizontal maps of ensemble-averaged changes in regressed DJF El Niño precipitation (shading, unit: mm day^{-1} K^{-1}) and SST (contours, unit: K K^{-1}) anomaly in three selected time slices in the CESM1.2 model. **d–o** as **a–c**, but for concurrent changes in major contributing moisture feedback processes (shading, unit: mm day^{-1} K^{-1}), including vertical advection of present-day background moisture by anomalous (**d–f**) shallow and (**g–i**) deep convective motion changes, **j–l** vertical advection of background moisture changes by present-day anomalous vertical motion, and **m–o** nonlinear change terms involving changes in both anomalous vertical motion and background moisture. The detailed meaning of each symbol is given in the Methods section. The Δ symbol indicates the ensemble-average change relative to the control simulation ensemble average. Stippled areas denote changes exceeding the 95% confidence level.

west zonally and are narrower meridionally, particularly during the La Niña phase. These biases can be attributed to model physics deficiencies[45] and a short observational record of strong ENSO events that is insufficient to constrain the model[46], but may be less influential in assessing relative changes in ENSO properties.

To assess precipitation-SST sensitivity changes, we selected three key time slices of 31 years each, centered at years 2079, 2149, and 2227, corresponding to half (2.6 K) and full (5.2 K) of the peak global mean surface temperature (GMST) changes (Fig. 1a). Different responses are found between strong El Niño and La Niña phases (Fig. 1b–g). Under global warming, El Niño precipitation sensitivity gradually intensifies and shifts eastward (Fig. 1d). As GMST peaks, the precipitation sensitivity center has shifted eastward by about 40° in longitude, accompanied by about a 30% increase in its magnitude of 1.5 mm day^{-1} (Fig. 1c; Supplementary Fig. 2e). The SST patterns show consistent changes, becoming stronger, zonally more contracted, but meridionally broader in the eastern Pacific (Fig. 1c). In addition, the stronger ENSO further depresses the negative precipitation anomaly in the western North Pacific, indicating a stronger low-level anticyclone. All of these changes are more evident when contrasted with the PD simulation (Fig. 2a, b).

Interestingly, in the CO_2 removal slice, when the GMST has returned to the same level as during the ramp-up phase (i.e., 2.6 K in 2227), El Niño precipitation sensitivity does not revert but instead continues its trend, with its center remaining anchored in the eastern Pacific around 120°W and showing even higher central values than in the GMST peak phase (Figs. 1b, c, 2b, c). This long El Niño hysteresis cannot be explained by the direct effect of global warming, but follows the evolution of the Pacific ITCZ centroid (Fig. 1a), suggesting a modulation of related circulation systems. Here, the hysteresis in the ITCZ centroid represents a systematic southward shift of the tropical Pacific background rain band during the CO_2 removal phase and is physically related to the atmospheric interhemispheric energy imbalance caused by the delayed Southern Ocean warming and the slow recovery of the Atlantic Meridional Overturning Circulation[33,47].

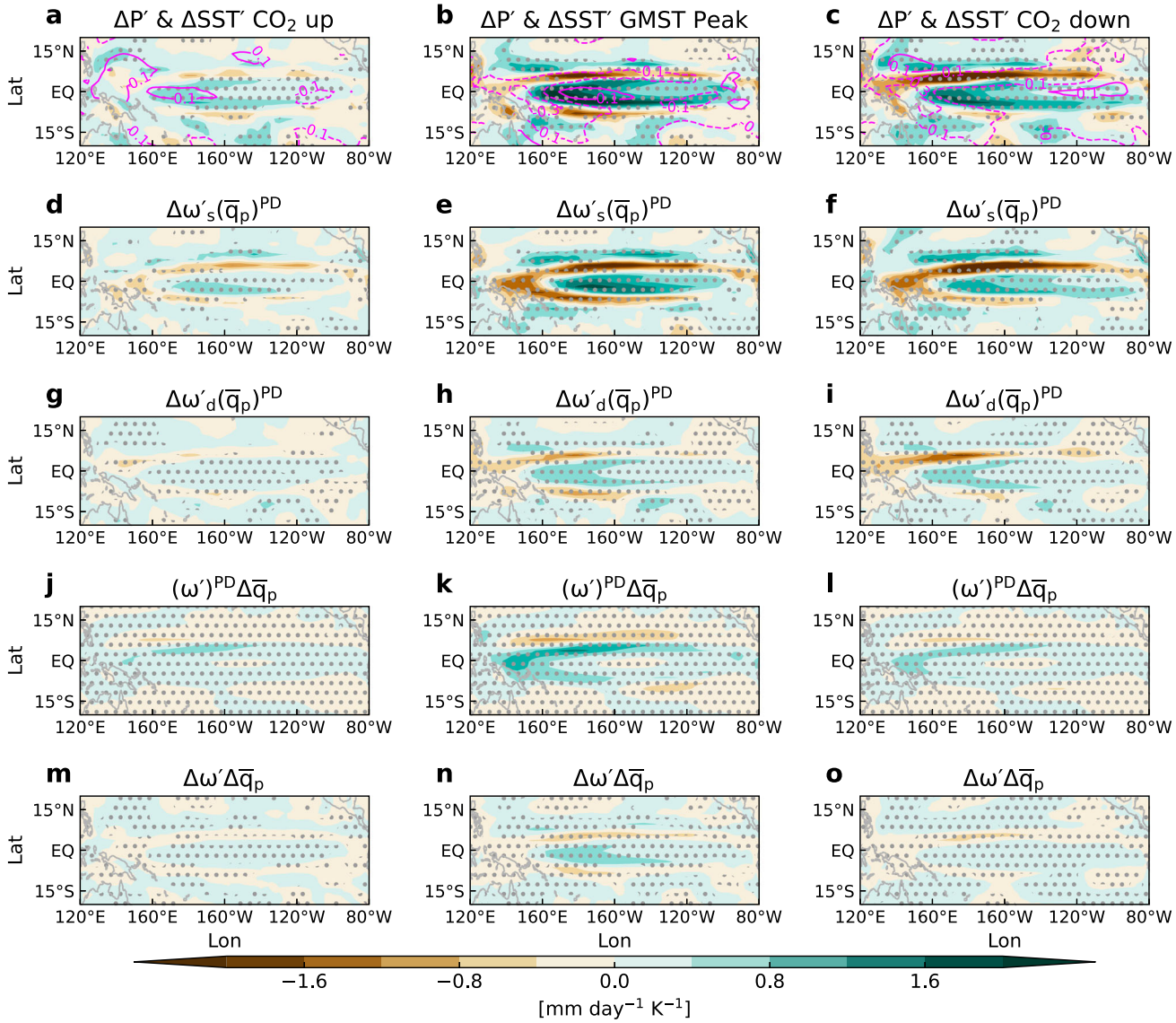


Fig. 3 | La Niña moisture budget. Same as Fig. 2, but for the strong La Niña case.

In contrast, the La Niña counterpart shows mostly structural changes rather than systematic zonal shifts (Fig. 1e–g). In the CO_2 increase slice, the precipitation sensitivity shows a meridional narrowing tendency with modest increases and decreases at the equator and off-equatorial regions, respectively, accompanied by a slightly enhanced equatorial SST anomaly (Figs. 1g, 3a). As the GMST peaks, such meridional narrowing changes become more pronounced and also appear in the SST field, showing a marked decrease in the equatorial western Pacific and a slight increase at the equator (Figs. 1f, 3b). In the CO_2 reduction slice, La Niña precipitation sensitivity changes generally recover, except for the negative changes north of the equator, which become even stronger. The SST anomaly retains its general structure, but the equatorial center shifts eastward into the eastern Pacific (Figs. 1e, 3c), possibly related to the concurrent eastward shift of the El Niño center. This leads to a recovery of the SST meridional contrast in the central-western Pacific. In short, La Niña precipitation sensitivity changes are more evident in the central-western Pacific and generally follow the global warming peak with some regional exceptions (i.e., north of the equator), showing a shorter hysteresis timescale of a few decades relative to the CO_2 forcing.

Moisture budget

Next, we use a moisture budget to understand ENSO precipitation sensitivity changes (Figs. 2, 3; Methods), expecting to identify key background-modulated feedback processes that shape ENSO hysteresis behavior. In the El Niño phase, the total changes in precipitation sensitivity ($\Delta P'$) show similar spatial structures of increasing magnitude across three time slices, manifesting as a broad zonal dipole structure of negative and positive changes in the equatorial western and eastern Pacific. The latter, along with positive changes in the off-equatorial central Pacific, form a lobster-like structure that retreats eastward (Fig. 2a–c). El Niño SSTs show consistent patterns of zonal dipole change, but do not align well with the detailed changes in precipitation sensitivity, suggesting their less straightforward role (see next section). On ENSO timescales, the tropical precipitation anomaly (P') is largely determined by the vertical advection of background moisture via anomalous convections ($\omega'\bar{q}_p$) (Supplementary Figs. 2, 3)[12]. Thus, future changes in this feedback ($\Delta(\omega'\bar{q}_p)$) are also of primary importance and can be further separated into changes in the anomalous vertical motion ($\Delta\omega'(\bar{q}_p)^{PD}$), the availability of background moisture ($(\omega')^{PD}\Delta\bar{q}_p$), and their nonlinear combinations ($\Delta\omega'\Delta\bar{q}_p$).

Our results show that changes in anomalous convection ($\Delta\omega'(\bar{q}_p)^{PD}$), which are separated into shallow ($\Delta\omega'_s$) and deep convection ($\Delta\omega'_d$) types given their fundamentally different dynamics (Supplementary Fig. 4; Methods), are critical for the total changes ($\Delta P'$; Figs. 2d–i, 3d–i). For the El Niño phase, the contribution of shallow convective anomalies ($\Delta\omega'_s(\bar{q}_p)^{PD}$) shows a meridional sandwich structure with a pronounced decrease and

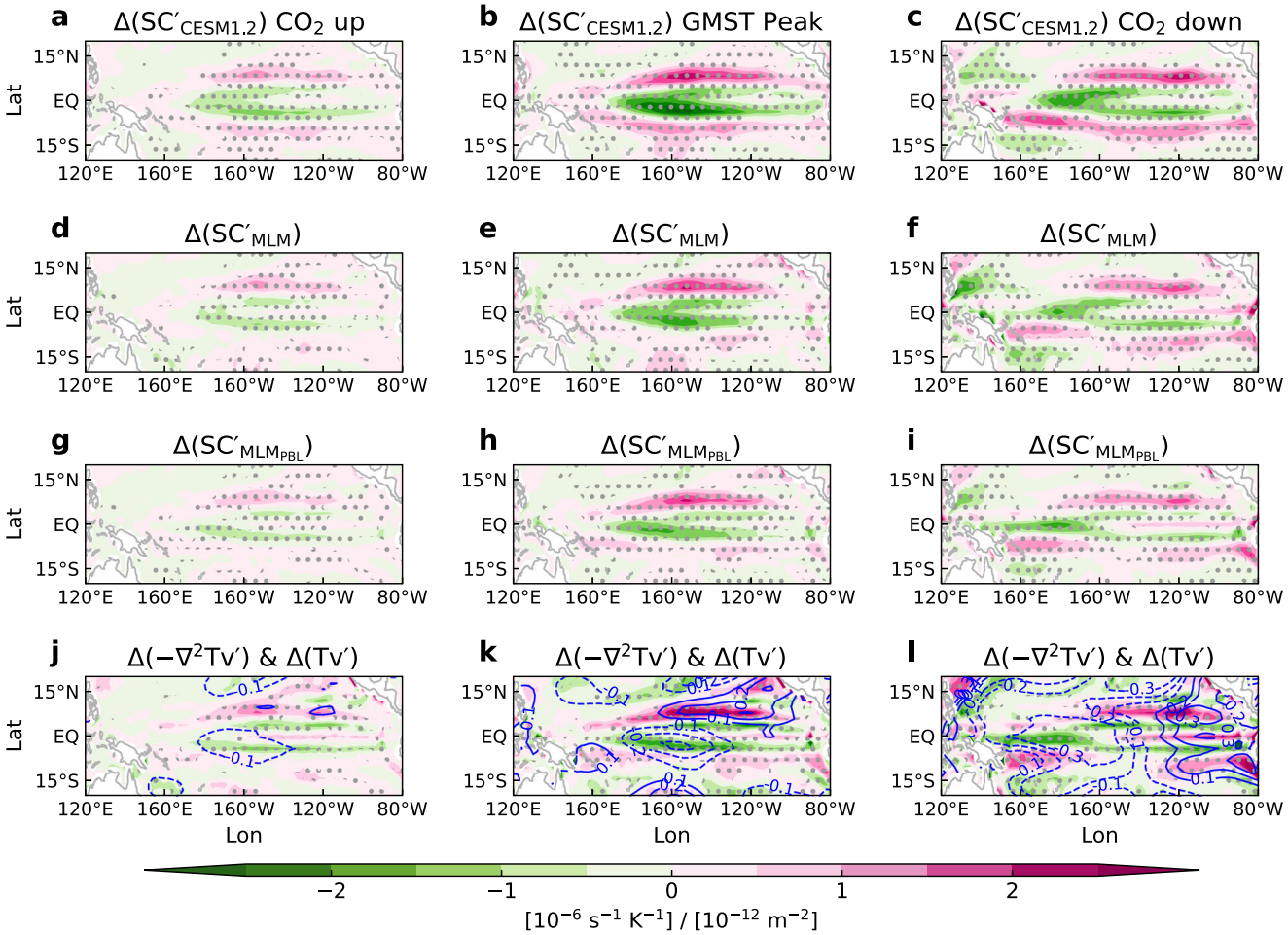


Fig. 4 | El Niño surface convergence changes. a–c Horizontal maps of ensemble-averaged changes in the regressed DJF El Niño 1000 hPa surface convergence anomaly (shading, unit: $s^{-1}\,K^{-1}$) in three selected time slices in the CESM1.2 model. **d–f** as **a–c**, but for surface convergence using a mixed-layer atmospheric model. **g–i** as **d–f**, but for mixed-layer model surface convergence anomaly contributed by boundary layer pressure component. **j–l** as **a–c**, but for the changes in boundary layer averaged virtual temperature (countours, unit: $K^{-1}\,K^{-1}$) and its Laplacian (shading, unit: m^{-2}). The Δ symbol indicates the ensemble-average change relative to the control simulation ensemble average. Stippled areas denote changes exceeding the 95% confidence level.

increase in the equatorial and off-equatorial central Pacific, respectively (Fig. 2d–f). Although it accounts for much of the total change, it intriguingly misses the key hysteresis features in the equatorial eastern Pacific, and thus cannot explain the eastward shift of equatorial El Niño precipitation sensitivity. Rather, this key hysteresis feature is related to deep convective term $(\Delta\omega'_d(\bar{q}_p)^{PD}$; Fig. 2g–i), which exhibits an equatorial zonal dipole structure of progressively decreasing and increasing precipitation sensitivity in the equatorial central and eastern Pacific. The changes in background moisture $((\omega')^{PD}\Delta\bar{q}_p)$ also favor an increased precipitation sensitivity over the equatorial central-eastern Pacific (Fig. 2j–l), but it shows a positive change maximum in the equatorial central Pacific due to the weighting of present-day El Niño-induced anomalous convection, with a magnitude following the GMST level under the thermodynamic Clausius-Clapeyron constraint. Both are less consistent with the spatial and temporal features of El Niño hysteresis. The nonlinear combination term $(\Delta\omega'\Delta\bar{q}_p)$ shows a zonal dipole structure following the changes in the anomalous vertical motion, but emphasizes more on the negative changes in the central Pacific and is comparatively weaker in its magnitude (Fig. 2m–o).

Other feedback terms (Supplementary Fig. 5) are secondary in explaining El Niño hysteresis. For example, changes in advection of moisture anomalies by background circulation $(\Delta(\bar{\vec{V}}_3\nabla_3 q'))$, showing a zonal dipole structure in the central-western North Pacific (Supplementary Figs. 5d–f), are dominated by its zonal component $(\Delta(\bar{u}q'_x)$; Supplementary Figs. 6a–i), which mainly involves changes in the zonal gradient of El Niño-driven moisture anomalies $((\bar{u})^{PD}\Delta q_x')$. The changes in the nonlinear advection term $(\Delta(\vec{V}_3{}'\nabla_3 q'))$, dominated by its vertical component $(\Delta(\omega' q'_p))$, contribute slightly to the El Niño hysteresis, mainly due to the eastward shifts of the El Niño-associated vertical motion and moisture anomalies (Supplementary Figs. 5g–i, 6j–r). Increased surface evaporation (Supplementary Fig. 5j–l) also has positive contributions in the equatorial eastern Pacific, but its hysteresis is mostly due to hysteresis changes in El Niño-associated anomalies rather than mean state modulations (see latent flux decomposition below). In short, while we acknowledge that all of these secondary feedbacks contribute to moisture budget closure, they are mostly consequential processes that accompany El Niño changes and thus provide less insight into the background state-modulated El Niño hysteresis.

The changes in La Niña precipitation sensitivity ($\Delta P'$) are more pronounced in the central-western Pacific, with a general increase in the equatorial region and meridional alternating negative and positive changes on either side in off-equatorial regions (Fig. 3a–c). Particularly, the equatorial changes peak in the GMST peak slice and attenuate in the subsequent CO_2 removal slice. The shallow convective terms $(\Delta\omega'_s(\bar{q}_p)^{PD})$ show very similar changes (Fig. 3d–f), suggesting its dominant role. Deep convective terms $(\Delta\omega'_d(\bar{q}_p)^{PD})$ roughly follow the spatial structures of the shallow type, but are smaller in magnitude (Fig. 3g–i). This comes from a dynamical coupling of shallow and deep convection[48], with the shallow type facilitating the development of the deep convection (see Eq. 7 in Methods). In contrast, the increased background moisture $((\omega')^{PD}\Delta\bar{q}_p$; Fig. 3j–l), weighted by the

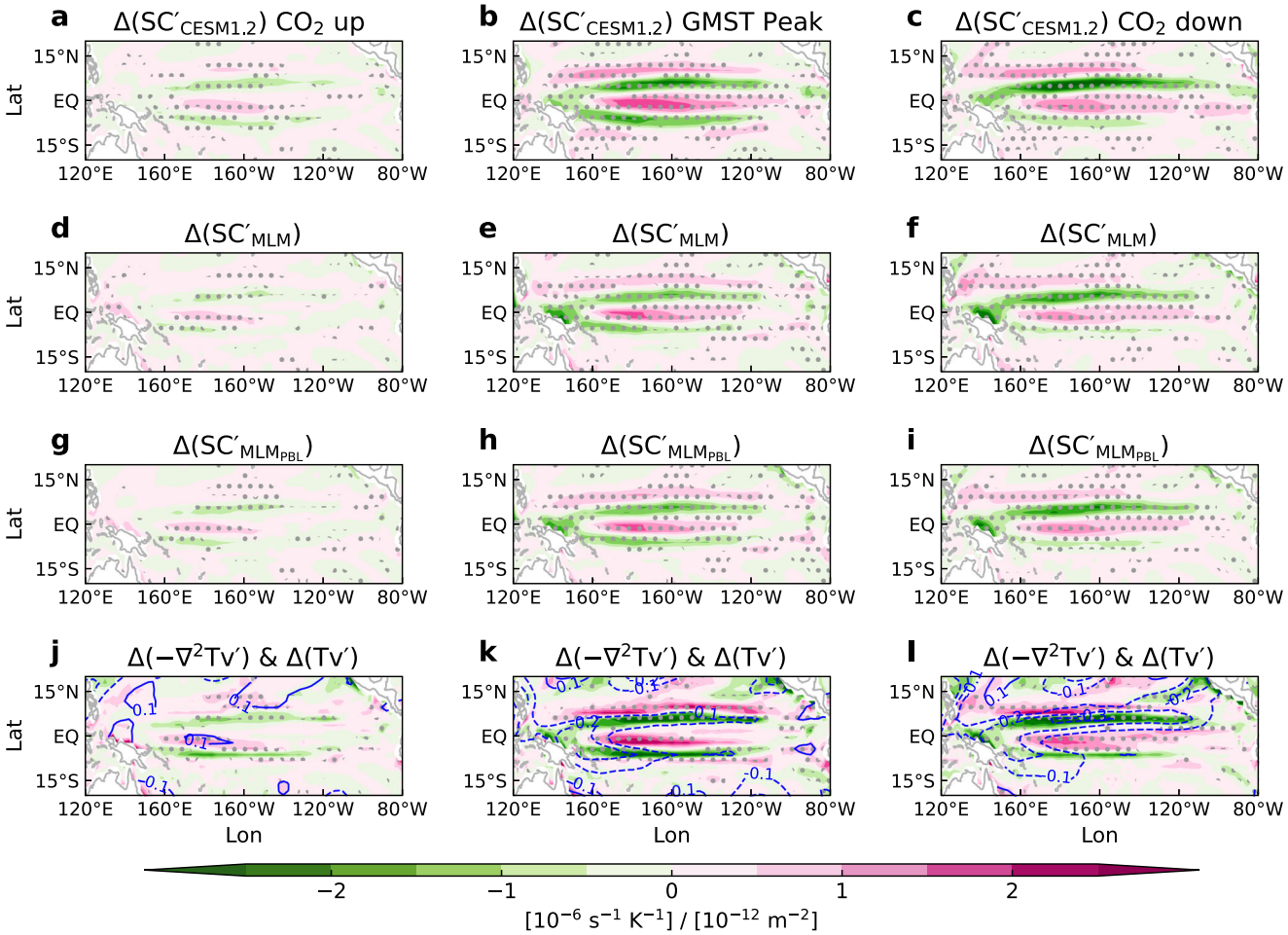


Fig. 5 | La Niña surface convergence changes. Same as Fig. 4, but the strong La Niña case.

current La Niña-induced anomalous vertical motion, favors a spatial expansion of precipitation sensitivity and thus contributes oppositely to the overall changes. The nonlinear combination term ($\Delta\omega'\Delta\bar{q}_p$; Fig. 3m–o) helps maximize changes in the equatorial central Pacific around the GMST peak, but it still relies on understanding changes in anomalous vertical motion. Other feedback processes are generally of secondary physical importance compared to the shallow convection term, and are provided for reference but not discussed for brevity (Supplementary Fig. 7).

Causes of shallow convective anomaly changes

In the following two sections, we use an atmospheric mixed-layer model (MLM) and MSE budget analysis to understand processes governing changes in anomalous shallow and deep convection. Shallow convection is largely driven by boundary layer wind convergence. Consistent with this understanding, the changes in the surface convergence anomaly at 1000 hPa (Figs. 4a–c, 5a–c) closely resemble the changes in shallow convective term in two ENSO phases (Figs. 2d–f, 3d–f). The MLM reproduces the overall structural changes of the surface convergence well, except for some biases around the coastal islands (e.g., Papua New Guinea) and some underestimation of the magnitude, especially in the central South Pacific (Figs. 4d–f, 5d–f). This may be due to several simplifying assumptions of the MLM framework and our direct adoption of model parameters tuned with early observations[23,49], but it does not affect our qualitative physical understanding.

An examination of each subcomponent contribution within the MLM framework (Methods) shows that the boundary layer pressure anomaly terms dominate the surface convergence changes (Figs. 4g–i, 5g–i), while the free tropospheric pressure anomaly and downward momentum mixing terms largely offset each other due to geostrophic balance at the boundary layer top[23] and thus have a small net effect (Supplementary Fig. 8). The ENSO SST anomaly shapes the boundary layer anomalous air temperature and humidity, whose collective effects on the pressure anomaly can be represented by the virtual temperature (*Tv*; Supplementary Fig. 9). In particular, the Laplacian of *Tv* ($\nabla^2 T_v$) has previously been suggested as a key factor for surface convergence in the MLM[41]. This is physically intuitive, since the gradient of *Tv* roughly represents the large-scale geostrophic winds.

Interestingly, despite similar patterns in boundary layer *Tv* and underlying SST anomalies (Supplementary Fig. 9), their future changes are not exactly the same. In the CO_2 increase and GMST peak slices, the El Niño SST changes emphasize zonal dipole structures (Fig. 2a, b), while the *Tv* changes are more pronounced in the equatorial central Pacific and subtropical northeast Pacific (Fig. 4j, k). This may be related to the locally high SST climatology, which amplifies the moisture response to even small SST perturbations and favors more turbulent activity that efficiently transports these surface anomalies upward. This *Tv* change pattern facilitates more evident surface convergence changes in the central Pacific than in the eastern Pacific (Fig. 4j, k). Similarly, during the CO_2 removal phase, the *Tv* change structure approaches the SST counterparts (Figs. 2c, 4l), but is more meridionally flattened in the eastern Pacific, resulting in small *Tv* Laplacian and surface convergence changes at the equator (Fig. 4l). On the other hand, the patterns of La Niña *Tv* changes resemble the corresponding SST changes (Figs. 3a–c, 5j–l), with negative changes in the equatorial western Pacific and adjacent off-equatorial regions acting to narrow the La Niña SST meridional extent. Taken together, the changes in the ENSO SST spatial distribution shape the shallow convective anomaly, but this is not necessarily a linear

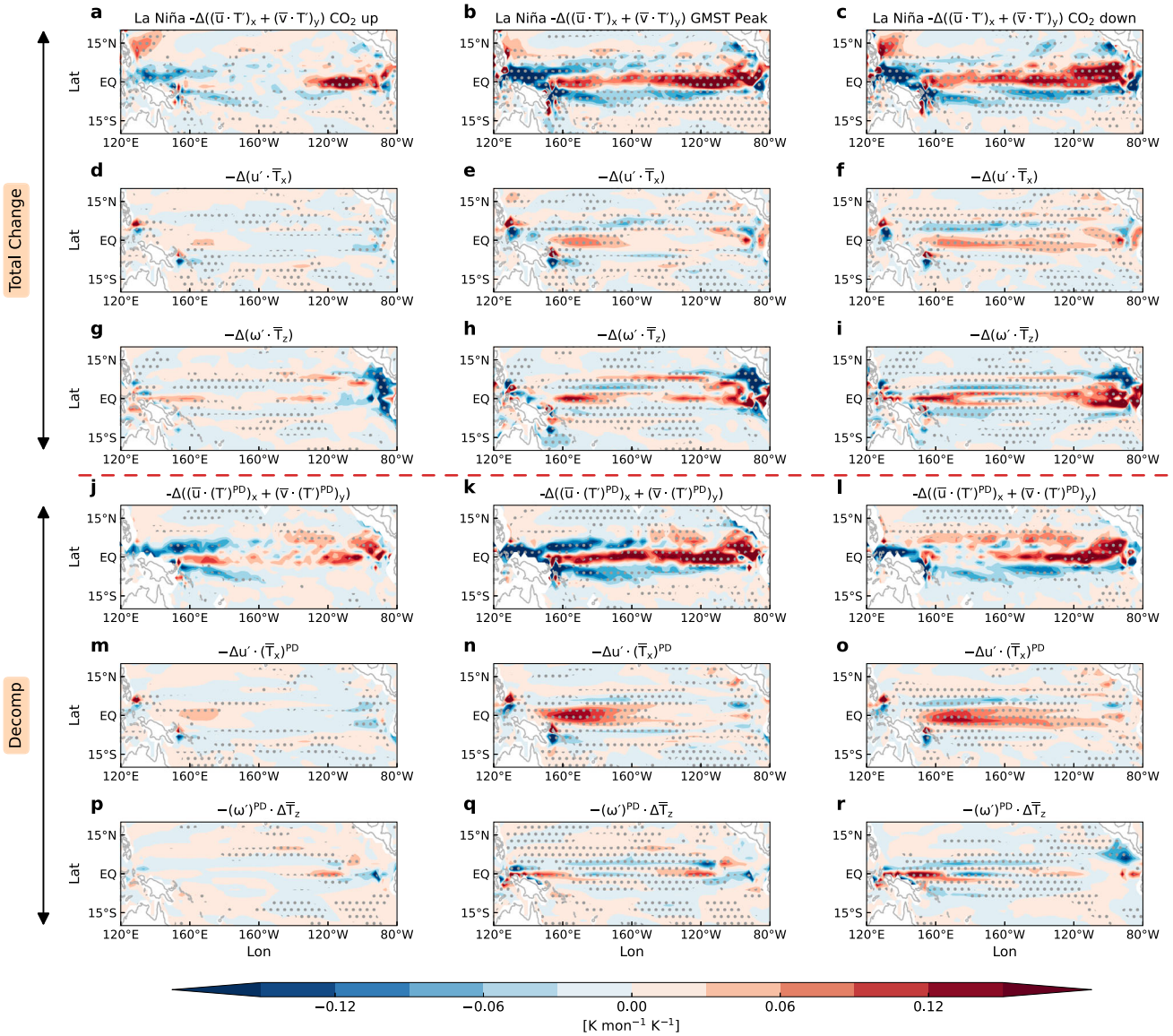


Fig. 6 | Key oceanic feedback for strong La Niña SST changes. Horizontal maps of ensemble-averaged changes in regressed DJF La Niña SST feedback processes (shading, unit: K mon^{-1} K^{-1}) in three selected time slices in the CESM1.2 model, including **a**–**c** dynamical damping term, **d**–**f** zonal advective feedback, and **g**–**i** Ekman feedback. **j**–**r** as **a**–**i**, but for the associated contribution term from changes in (**j**–**l**) background ocean current, **m**–**o** La Niña-induced zonal current anomalies, and **p**–**r** vertical gradient of background ocean temperature. The Δ symbol indicates the ensemble-average change relative to the control simulation ensemble average. Stippled areas denote changes exceeding the 95% confidence level.

mapping, as the ultimate atmospheric responses also depend on detailed boundary layer processes.

According to our previous studies[30,31], ENSO SST changes are a consequence of coupled ocean-atmosphere feedback changes that are ultimately modulated by the ocean-atmosphere background conditions. The eastward shift of El Niño SST is directly due to enhanced positive oceanic feedback in the eastern Pacific (e.g., thermocline feedback). However, this process is largely internal to El Niño and show less evidence of direct hysteresis modulation by background ocean conditions (e.g., stratification, thermocline depth, etc.). Rather, the strong El Niño SST changes are more likely rooted in the atmospheric ITCZ, given their similar hysteresis evolution. Physically, as will be shown below, ITCZ hysteresis enhances cloud-longwave feedback and deep convective motions in the equatorial eastern Pacific. The associated stronger wind stress anomaly response can drive stronger oceanic feedback to amplify the El Niño SST anomaly, shift the El Niño center eastward, and cause changes in shallow convection anomalies. Note that in our MLM analysis, the SST anomaly is treated as a prescribed external forcing, whereas in reality, it interacts with the atmospheric response to produce the final observed changes.

Strong La Niña SSTs are more directly influenced by changes in the background ocean conditions[31]. A mixed-layer ocean heat budget (Fig. 6; Methods), shows that changes in horizontal advection of anomalous SSTs by the mean ocean current (i.e., dynamical damping term, Fig. 6a–c) explain most of the La Niña SST structure changes over the central-western Pacific, compared to other feedback processes (Fig. 6d–i; Supplementary Fig. 10). A further decomposition highlights the role of background ocean current changes, especially under global warming time slices. This suggests an ocean circulation-modulated La Niña SST structure and precipitation sensitivity, aligning somewhat with a previous study based on the HadCM3C model[17], although in their case the mechanism is more applicable to the El Niño phase. Interestingly, in the CO_2 reduction slice, La Niña SST still shows negative changes north of the equator (Fig. 3c), but the local dynamical damping term is muted (Fig. 6c) due to the offsetting effects between changes in the mean circulation and La Niña SST (Fig. 6l; Supplementary Fig. 11c). Instead, these north equatorial SST changes may be due to

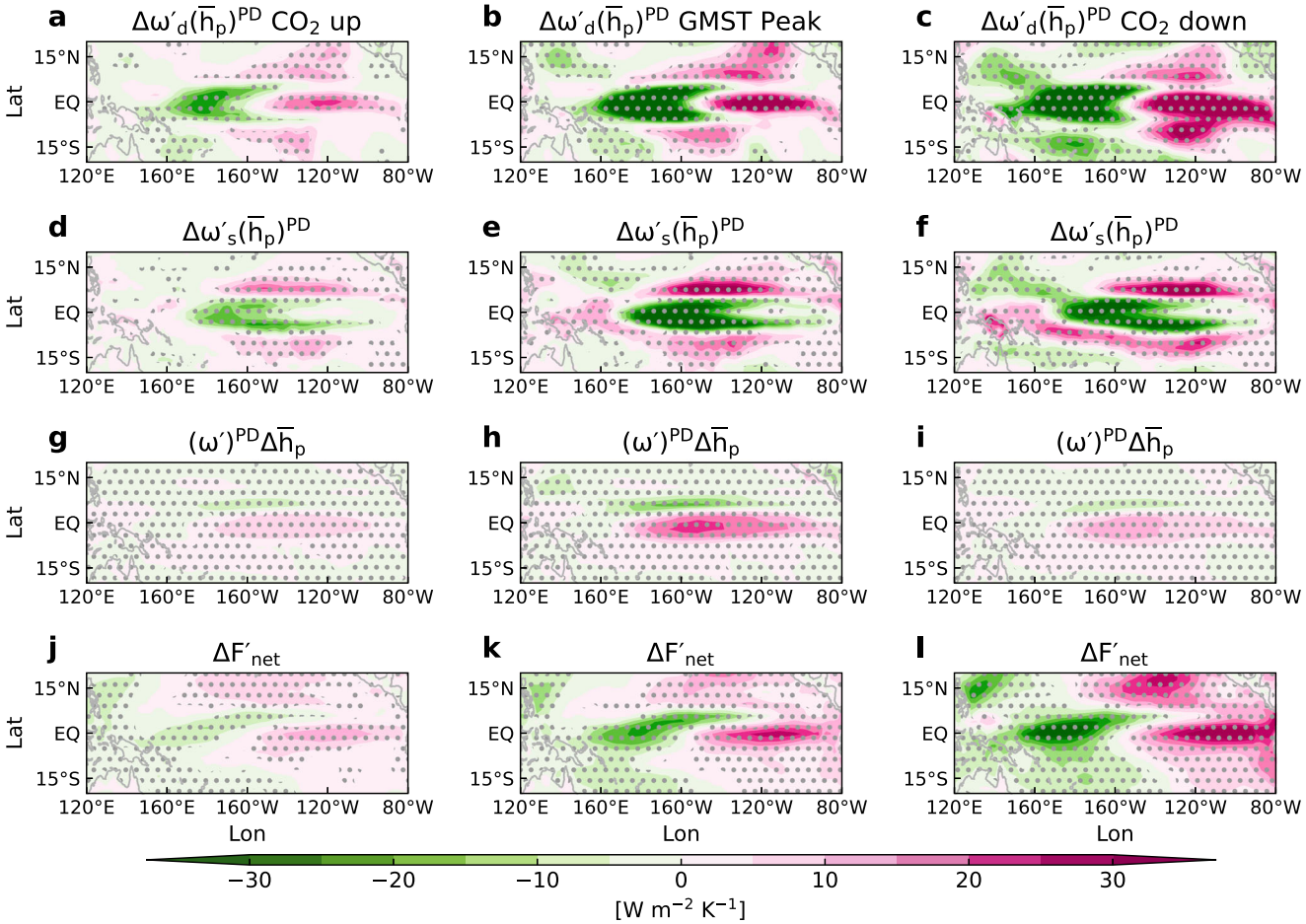


Fig. 7 | Key MSE feedback for strong El Niño deep convective anomaly changes. **a**–**c** Horizontal maps of ensemble-averaged changes in regressed DJF El Niño vertical advection of present-day background MSE by anomalous deep convection changes (shading, unit: W m^{-2} K^{-1}) in three selected time slices in the CESM1.2 model. **d**–**l** as **a**–**c**, but for concurrent changes in major contributing MSE feedback processes (shading, unit: mm day^{-1} K^{-1}), including vertical advection of present-day background MSE by anomalous **d**–**f** shallow convective motion changes, **g**–**i** vertical advection of background MSE changes by present-day anomalous vertical motion, and **j**–**l** net heat flux feedback. The detailed meaning of each symbol is available in the Methods section. The Δ symbol indicates the ensemble-average change relative to the control simulation ensemble average. Stippled areas denote changes exceeding the 95% confidence level.

progressively stronger negative changes in zonal advection and the Ekman feedback (Fig. 6f, i), which are mainly contributed by local changes in the La Niña zonal current (Fig. 6o; Supplementary Fig. 11d–f) and the vertical gradient of the background ocean temperature (Fig. 6r; Supplementary Fig. 11g–i), respectively. Both may be related to the enhanced thermal contrast between the sea surface and the mixed-layer bottom (see last section), which enhances local vertical stratification and ocean wave response, and facilitates more efficient de-entrainment of mixed-layer ocean temperature anomalies. Note that these two processes are complementary to the dominant effects of the ocean mean circulation, as the strongest changes in the La Niña SST meridional gradient and equatorial shallow convection anomalies occur in the GMST peak slice (Fig. 3a–c).

Causes of deep convective anomaly changes

Next, we use an MSE budget (Methods) to understand deep convective anomaly changes, with particular attention to the El Niño phase, where it plays a critical role (Fig. 7). Since the MSE budget combines the moisture and temperature equations, most of its feedback changes have similar characteristics to the moisture budget case and are easy to understand by analogy. The deep convective terms ($\Delta\omega'_d(\bar{h}_p)^{PD}$) show zonal dipole structures of increasing magnitude (Fig. 7a–c), similar to the deep convective precipitation changes (Fig. 2g–i), and are mainly contributed by the net heat flux term ($\Delta F'_{net}$; Fig. 7j–l). Like the moisture budget case, the shallow convective term ($\Delta\omega'_s(\bar{h}_p)^{PD}$; Fig. 7d–f), characterized by a meridional sandwich structure in the central Pacific, contributes to local deep convective motion, but has less effect in the far eastern Pacific. The background MSE term ($(\omega')^{PD}\Delta\bar{h}_p$; Fig. 7g–i) shows a maximum positive center in the equatorial central Pacific in the GMST peak slice, inconsistent with spatial and temporal features of El Niño hysteresis. As in the moisture budget case, other terms are less important (Supplementary Fig. 12). For instance, changes in the horizontal advection of enthalpy anomalies by the background circulation ($\Delta(\bar{\vec{V}}_2\nabla_2 k')$; Supplementary Fig. 12d–f) are dominated by its zonal component ($\Delta(\bar{u}k_x')$) associated with the zonal gradient changes in El Niño-driven enthalpy anomalies ($(\bar{u})^{PD}\Delta k_x'$; Supplementary Fig. 13). The nonlinear vertical advection term ($\Delta(\omega' h')$; Supplementary Fig. 12p–r) shows a zonal dipole structure in the CO_2 removal phase and contributes to some El Niño hysteresis, but is a consequence of the eastward shift of the El Niño-driven vertical motion and MSE anomalies.

The most important net heat flux term is dominated by the longwave and surface latent heat flux components, while the shortwave and sensible heat flux terms are negligible (Fig. 8a–f; Supplementary Fig. 14a–f). The longwave feedback is dominated by the cloud component, while the clear-sky component showing a similar pattern of lower magnitude (Supplementary Fig. 14g–l). Here, zonal dipole structures are due to the eastward shift of El Niño, which increases cloud, moisture, and longwave radiation anomalies in the east and decreases them in the central Pacific. For the cloud component, its sensitivity to cloud perturbations depends on the background cloudiness, especially the high cloud type, which shows a strong

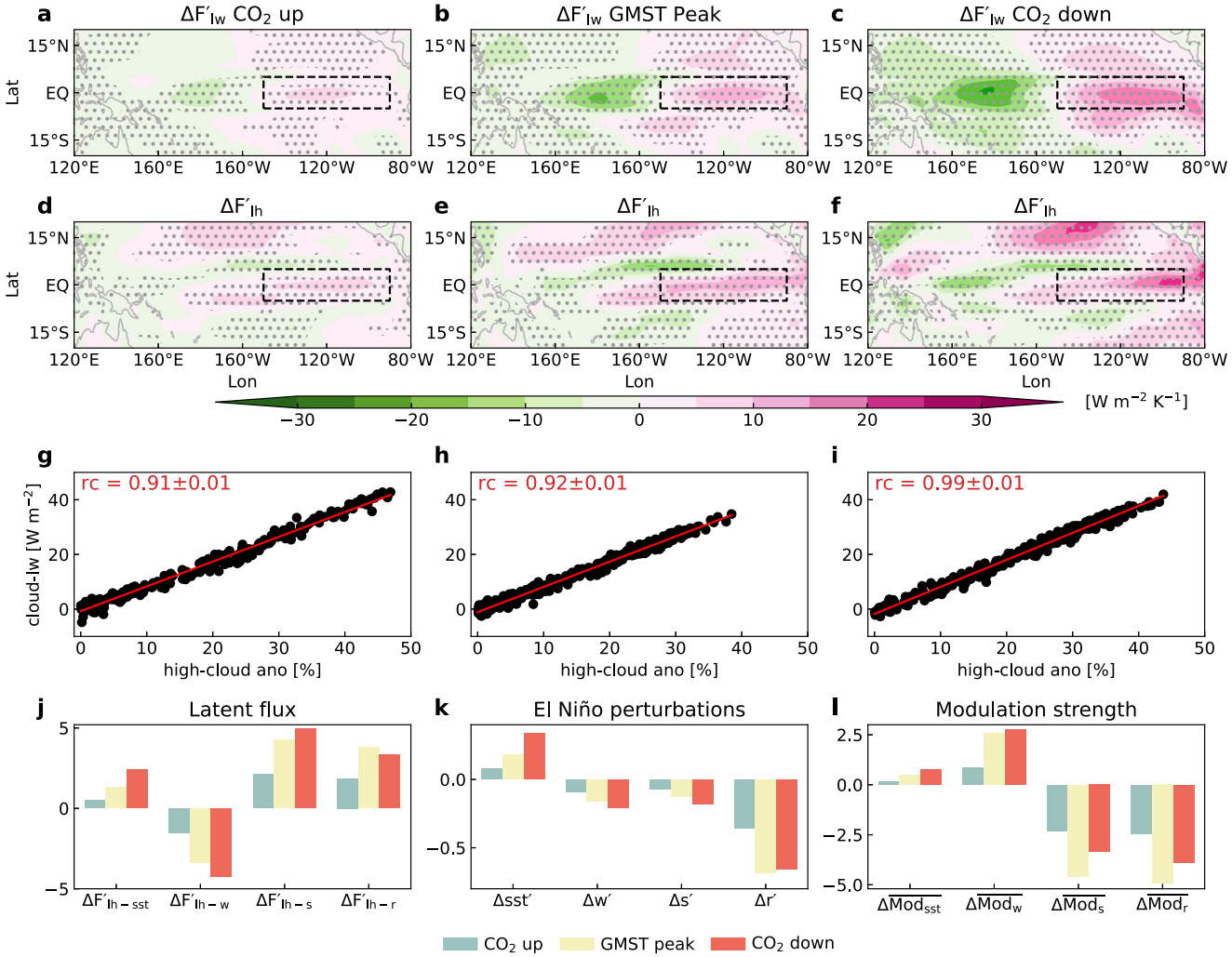


Fig. 8 | Decomposition of strong El Niño net heat flux. Horizontal maps of ensemble-averaged changes in regressed DJF El Niño (a–**c**) net longwave anomaly (shading, unit: W m^{-2} K^{-1}) and **d**–**f** net surface latent heat flux (shading, unit: W m^{-2} K^{-1}) in three selected time slices in the CESM1.2 model. **g**–**i** Scatter plots of the equatorial eastern Pacific (90°-150°W, 5°S-5°N, black box) DJF high cloud anomaly (unit: %) and cloud longwave radiation anomalies (unit: W m^{-2}) under El Niño conditions for three selected time slices. The regression coefficient is also given in each subplot. **j** Bar plots of the DJF El Niño equatorial eastern Pacific latent heat anomaly contributed by four subcomponents involving changes in SST anomaly, surface wind speed anomaly, surface stability, and relative humidity. Green, yellow, and red bars represent CO_2 ramp-up, GMST peak, and CO_2 ramp-down slices. **k** and **l** are similar to **j**, but for **k** the changes in El Niño-induced physical perturbations, and **l** for the corresponding mean state modulation strength. More details on latent heat flux decomposition are given in the Methods section. The Δ symbol indicates the ensemble-average change relative to the control simulation ensemble average. Stippled areas denote changes exceeding the 95% confidence level.

hysteresis increase over the equatorial central-eastern Pacific following ITCZ changes (Fig. 9). Physically, the denser clouds allow more effective retention of longwave radiation anomalies by the same cloud anomalies (Fig. 8g–i). Instead, the clear sky component is accompanied by El Niño hysteresis, as the eastward shift of El Niño increases the water vapor anomaly in the eastern Pacific and traps more longwave anomalies via its greenhouse effect[50], and the opposite occurs in the central Pacific.

The eastern Pacific surface latent heat flux also plays a role in El Niño precipitation sensitivity hysteresis, increasing the local deep convective anomaly in the MSE budget and surface evaporation in the moisture budget (Supplementary Fig. 5j–l). Because it typically mixes the SST response and atmospheric forcing of multiple processes[51,52], we separate its changes into subcomponents related to SST, wind speed, relative humidity, and stability anomalies, and assess their respective background state modulation strengths (Methods). The total latent flux changes are contributed, in descending order of importance, by the stability, relative humidity, and SST terms, while the wind term has an opposite effect (Fig. 8j). Interestingly, however, the hysteresis is mainly in changes in their El Niño-induced anomalies (Fig. 8k), while the corresponding modulation coefficients peak in the GMST peak slice (Fig. 8l). This suggests that the surface latent heat flux is more of a positive feedback associated with El Niño changes, but less of a cause subject to direct background hysteresis modulation.

In the La Niña phase, the deep convective term $(\Delta\omega_d'(\bar{q}_p)^{PD})$ is secondary compared to the shallow convective term in the moisture diagnosis (Fig. 3d–i), so we briefly discuss the associated energy budget for completeness (Supplementary Fig. 15). The deep convective anomaly changes $(\Delta\omega_d'(\bar{h}_p)^{PD})$ are mostly driven by the shallow convective changes $(\Delta\omega_s'(\bar{h}_p)^{PD})$ due to their dynamical coupling[48] (see Eq. 7 in Methods), further emphasizing the SST structural changes in the La Niña hysteresis. The net flux term also has some contribution, but is secondary and may be modulated by changes in middle cloudiness, which extends farther west into the western Pacific and peaks earlier in the GMST peak phase than the high cloud type (Fig. 9g–i). Other MSE terms are not considered for their even smaller contribution to this secondary deep convective process. In short, background atmospheric conditions in the central-western Pacific (e.g., clouds and moisture), while contributing to La Niña precipitation sensitivity

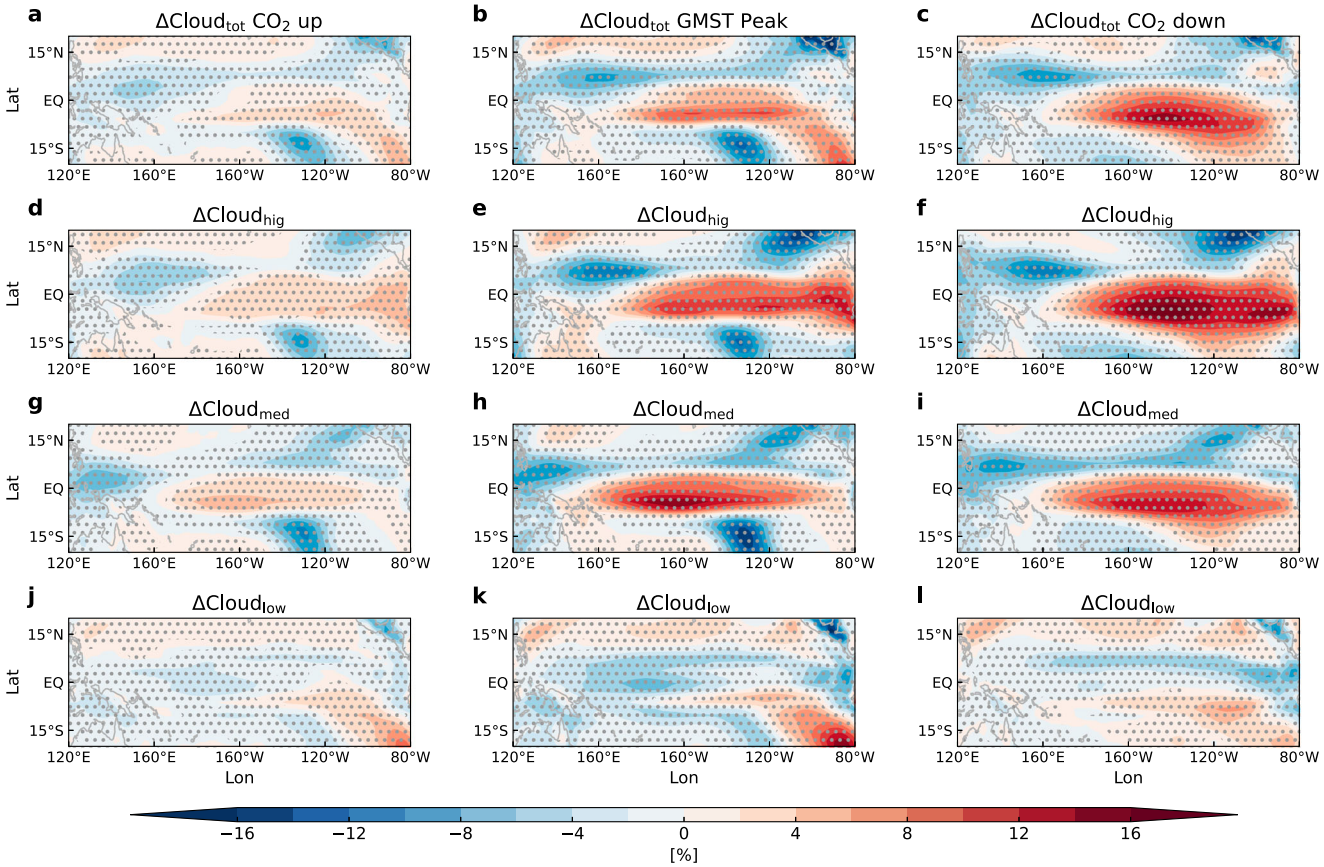


Fig. 9 | Changes in background clouds. Horizontal maps of ensemble-averaged changes in DJF background **a**–**c** total cloudiness (shading, unit: %); **d**–**f** high cloudiness (shading, unit: %); **g**–**i** middle cloudiness (shading, unit: %); and **j**–**l** low cloudiness (shading, unit: %) in three selected time slices in the CESM1.2 model. The Δ symbol indicates the ensemble-average change relative to the control simulation ensemble average. Stippled areas denote changes exceeding the 95% confidence level.

changes, may be less fundamental compared to the ocean-modulated La Niña SST structure and shallow convection changes.

Changes in key ocean-atmosphere mean states

Our diagnosis suggests key modulating systems of ITCZ-associated eastern Pacific cloudiness and western Pacific upper-ocean conditions for strong ENSO precipitation sensitivity. We next discussed their physical processes. Under global warming, tropical Pacific SSTs show an overall increase, with the eastern Pacific increasing more than the western Pacific (Fig. 10a–c). This El Niño-like warming pattern is crucial for regional atmospheric responses and is more evident in the relative SST (RSST; Fig. 10d–f), the local SST difference from the tropical mean SST (20°S-20°N). For example, it can influence either the gross moist stability and/or the atmospheric low-level warming and associated moisture flux convergence to cause an increase in equatorial mean precipitation (here cloudiness) via the warmer-gets-wetter or the Laplacian-of-warming mechanisms[41,51]. Despite different physical processes emphasized, both mechanisms recognize the importance of the SST warming pattern and are generally supported by similar large-scale patterns between relative SST, moisture flux convergence, and cloudiness changes here (Figs. 9, 10d–i), so we do not strictly distinguish their differences here.

After the GMST peak, the SST change recovers, but the warming pattern becomes even more pronounced (Fig. 10c, f) likely due to the slow oceanic adjustment processes[53,54]. In particular, the positive RSST is more dominant in the Southern Hemisphere, creating an interhemispheric thermal contrast in the central-eastern Pacific accompanied by a southward shift of the ITCZ. This causes cross-equatorial northerly winds and a southward displacement of the equatorial zonal westerlies. Similar changes are reflected in moisture fluxes (Fig. 10i), whose convergence increases convection and cloudiness in the near-equatorial regions of the Southern Hemisphere. Meanwhile, the slow recovery of the Atlantic Meridional Overturning Circulation during the CO_2 removal phase also contributes to the interhemispheric energy imbalance and ITCZ hysteresis by reducing northward ocean heat transport and thus a warmer Southern Hemisphere[33,47].

In contrast to the pronounced hysteresis in the eastern Pacific ITCZ, the upper-ocean circulations see the largest changes in the GMST peak slice (Fig. 10j–l). Under global warming, there are eastward and westward zonal current changes in equatorial and off-equatorial regions, corresponding to a strengthening of the equatorial countercurrent and the south and north equatorial currents, respectively. This is explained by the thermodynamically enhanced upper-ocean stratification, which closely follows the SST warming magnitude, with the warming pattern being less important[55]. In addition, the equatorial westerlies drive an equatorward inflow of meridional Ekman currents from both hemispheres, indicating a weakening of the Pacific subtropical cell[21]. These ocean currents act to squeeze the La Niña SST structure and shape La Niña precipitation sensitivity. In the CO_2 reduction slice, the southward shift of equatorial zonal winds weakens or even reverses the meridional ocean current change in the Northern Hemisphere, while strengthening it in the Southern Hemisphere, weakening its overall influences on La Niña SST structure.

In addition to mixed-layer ocean currents, vertical ocean thermal structures in the western Pacific may also play a complementary role in prolonging negative La Niña SST changes north of the equator in the CO_2 removal slice by modulating zonal advective and Ekman feedbacks. In particular, the thermal contrast between the 50 m ocean and the sea surface shows the largest enhancement (i.e., negative changes) in the CO_2 reduction slice (Fig. 10m–o), indicating faster subsurface cooling than the surface. This may be related to the hysteresis of the El Niño-like warming pattern, whose surface winds drain the heat content of the western Pacific, likey through

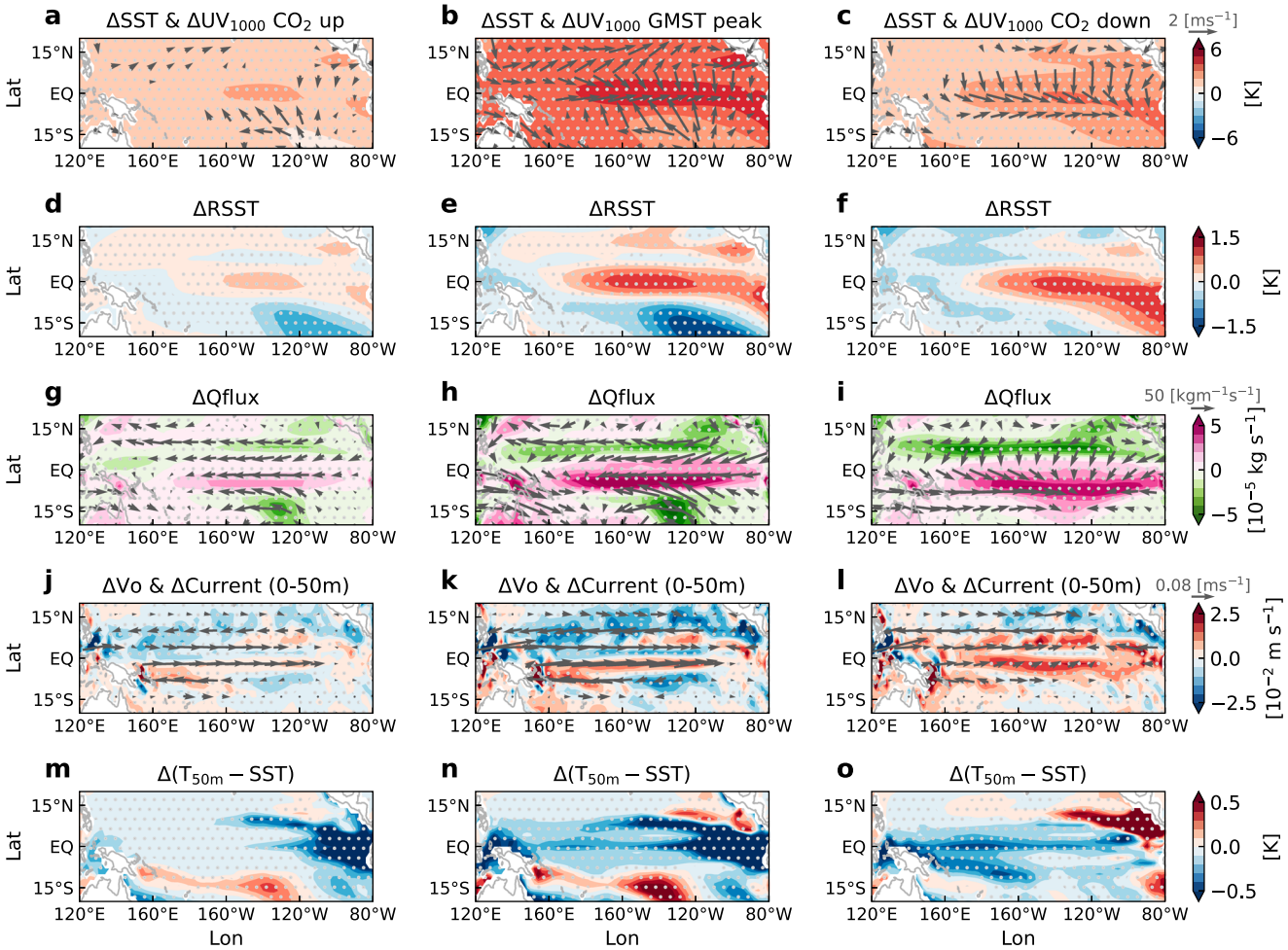


Fig. 10 | Changes in ocean-atmosphere mean states. Horizontal maps of ensemble-averaged changes in DJF (**a**–**c**) SST (shading, unit: K) and 1000 hPa wind (vector, unit: m s^{-1}); (**d**–**f**) relative SST (shading, unit: K); (**g**–**i**) moisture flux (vector, unit: kg m s^{-1}) and associated moisture flux convergence (contours, unit: 10^{-5} kg s^{-1}); (**j**–**l**) mixed-layer ocean current (vector, unit: m s^{-1}) and meridional current (shading, unit: m s^{-1}) component; and (**m**–**o**) seawater temperature contrast (shading, unit: K) between 50 m and sea surface in three selected time slices in the CESM1.2 model. The Δ symbol indicates the ensemble-average change relative to the control simulation ensemble average. Stippled areas denote changes exceeding the 95% confidence level.

ocean wave processes, allowing the subsurface water to exert more influence around the mixed layer bottom and ultimately shaping the local upper-ocean thermal structure and La Niña SSTs.

Discussion

Using CESM1.2 large ensemble simulations under an idealized 1% $year^{-1}$ CO_2 ramp-up to quadrupling and a subsequent symmetric ramp-down path, we show different hysteresis responses of strong El Niño and La Niña precipitation-SST sensitivity. The strong El Niño precipitation sensitivity progressively intensifies and shifts eastward under global warming and maintains such changes through the middle of the CO_2 ramp-down phase, showing strong hysteresis behavior on a timescale comparable to the CO_2 forcing (i.e., multi-decadal to century), while the La Niña counterpart is less pronounced and mostly confined to the central-western Pacific, with a hysteresis change of a few decades. Detailed budget diagnostics show that the strong El Niño hysteresis has an atmospheric root in the eastern Pacific ITCZ. Its southward shift during the CO_2 removal phase increases the high cloudiness near the equator, which favors the destabilization and establishment of deep convective anomalies by increasing the outgoing longwave retention efficiency of the air column. With the changes in the deep convective anomaly, the resulting atmospheric circulation changes drive El Niño SST changes via triggering oceanic feedbacks, which further cause changes in shallow convective precipitation sensitivity around the central Pacific. All of these ocean-atmospheric changing processes are interactively amplified to form the final forced responses. In contrast, the La Niña counterpart in the central-western Pacific relies more on the shallow convective type determined by the La Niña SST structures, which are mainly modulated by the changes in the upper-ocean background circulations due to ocean warming, and thus have shorter hysteresis timescales of a few decades.

The important role of the eastern Pacific background ITCZ in shaping strong El Niño precipitation-SST sensitivity in our CO_2 removal experiment is in line with previous findings and thus provides a reference mechanism in other climate change conditions, including the observed El Niño regime shift[56], extreme convective El Niño responses to greenhouse warming[11], ENSO responses to volcanic eruptions[57] or Arctic air-sea interactions[40], and past ENSO activity variation due to orbit changes[58]. For example, in our study, the hysteretic southward movement of the eastern Pacific ITCZ, which shifts El Niño convection and variability to the eastern Pacific, can be viewed as an inverse situation to that reported by Hu and Fedorov[56], who showed that cross-equatorial low-level northward winds reduce El Niño variability in the eastern Pacific, potentially explaining the recently observed changes in ENSO regime.

To assess the uncertainty in our results, we also analyzed eight available Coupled Model Intercomparison Project Phase 6 (CMIP6)[59,60] models under a similar CO_2 pathway (Supplementary Figs. 16, 17; Methods). For the strong El Niño phase, the precipitation-SST sensitivity in the piControl

simulation of all eight models is primarily confined to the central-western equatorial Pacific, with an evident underestimation in the far-eastern Pacific due to the cold tongue cooling bias[45]. Among them, the CESM2 and NorESM2-LM models with more eastward precipitation centers show positive hysteresis changes in the equatorial eastern Pacific and negative changes around the central Pacific, which is somewhat similar to the CESM1.2 case, thus supporting our results in a loose sense (Supplementary Fig. 16a, c, h). The MIROC-ES2L model (Supplementary Fig. 16g) also shows some ability to capture strong El Niño dynamics and an eastward shift of future precipitation, but its hysteresis change is opposite to the CESM1.2 case (Supplementary Fig. 16a), being stronger in the CO_2 ramp-up phase than in the ramp-down phase. This may be due to a less pronounced hysteresis of the background ITCZ in this model[30] and/or the single ensemble member. For other models (Supplementary Fig. 16b, d–f, i), the westward precipitation may allow them to escape modulation by the eastern Pacific ITCZ, making hysteresis changes less pronounced and more in the central Pacific.

For the strong La Niña phase, the CESM2 model generally supports our findings and shows the most pronounced changes in precipitation sensitivity, with hysteresis features (e.g., equatorward narrowing and maximization in the GMST peak) and SST structures generally similar to its previous version (i.e., CESM1.2; Supplementary Fig. 17a, c). The precipitation sensitivity changes in other models are mostly scattered and less systematic, potentially due to biased SST dynamics. This is evidenced by the eastern Pacific La Niña SST centers in the piControl simulation of these models, which are located in the central-western Pacific in the observational and CESM models (Supplementary Figs. 2, 17). The biased SST dynamics hinder a faithful future projection of La Niña SST structure and associated shallow convection anomalies. Furthermore, a single available ensemble member is also blamed for the above intermodel uncertainties, containing insufficient ENSO samples to well separate forced changes from internal variability. In this context, we note that our CESM1.2-based results, although subject to some model dependence, may still be trustworthy given its outperformance in simulating strong ENSO features compared to other models. Due to multiple competing feedback processes involved in ENSO and their dedicated balances, we suggest that future large ensemble simulations using different climate models with improved model physics (e.g., convective parameterization scheme) and reduced mean state bias are necessary to provide reliable future projections of ENSO precipitation characteristics, atmospheric teleconnections, and their mean state forcers.

Methods

Model experimental design

In our study, we use a large ensemble simulation output of the Community Earth System Model version 1.2 (CESM1.2)[35], which has a reasonable ability to simulate key air-sea coupling characteristics of ENSO and has been widely used in previous studies[39,61–63]. An idealized ramp-up and ramp-down trajectory of CO_2 forcing is prescribed to mimic conditions of anthropogenic warming and subsequent climate change mitigation. Specifically, from a prescribed initial level of 367 ppmv ($1 \times CO_2$) around the year 2000, the CO_2 concentration increases linearly at a rate of 1% $year^{-1}$ for a 140-year ramp-up period until it quadruples ($4 \times CO_2$, 1468 ppmv), followed by a symmetric decrease of 1% $year^{-1}$ for another 140-year ramp-down period until it returns to the initial level and is held constant for an additional 220-year restoring period. This CO_2 forcing is applied to 28 ensemble members, each with different initial conditions. In addition, a 900-year present-day (PD) control simulation with fixed CO_2 concentration at the baseline level ($1 \times CO_2$) is used as a baseline to assess climate change effects. More details on the model configurations and experimental designs can also be found in our previous literature[30,31,47].

Datasets

To evaluate the model performance of CESM1.2 in simulating the strong ENSO precipitation characteristics and associated moisture feedback processes, we also used the monthly mean SST and atmospheric circulation data from the fifth generation of the European Centre for Medium-Range Weather Forecasts (ECMWF) reanalysis (ERA5)[64]. The analysis period spans from 1979 to 2022 to ensure high data quality.

In addition, eight available climate models participating in the Coupled Model Intercomparison Project Phase 6 (CMIP6)[59] are used for comparison with our CESM1.2 model results to provide information on intermodel uncertainties. Namely, ACCESS-ESM1-5 (r1i1p1f1), CESM2 (r1i1p1f1), CNRM-ESM2-1 (r1i1p1f2), CanESM5 (r1i1p2f1), GFDL-ESM4 (r1i1p1f1), MIROC-ES2L (r1i1p1f2), NorESM2-LM (r1i1p1f1), and UKESM1-0-LL (r1i1p1f2). The first 500 years of each model's preindustrial control (piControl) simulation are used as a reference run. The CO_2 ramp-up and ramp-down periods are composed of the "1pctCO_2" experiment from the CMIP6 Diagnostic, Evaluation, and Characterization of Klima[59] and the "1pctCO_2-cdr" experiment from the Carbon Dioxide Removal Model Intercomparison Project (CDRMIP)[60], respectively. Each model includes only one ensemble member across all three experiments, with realization labels indicated in parentheses following the model name. For the CO_2 ramp-up and ramp-down experiments, the temporal evolution of CO_2 concentration follows that in the CESM1.2 model, with a slightly different initial pre-industrial CO_2 concentration (284.7 ppmv) and a resulting quadrupled peak value ($4 \times CO_2$, 1138.8 ppmv).

ENSO precipitation-SST sensitivity and statistical analysis

We focus on the boreal winter season from December to February (DJF), when ENSO matures and the atmospheric response is strongest. Considering the pronounced ENSO asymmetry, the El Niño and La Niña induced equatorial precipitation anomalies are estimated separately by an ENSO phase-dependent asymmetric regression method[42], where the anomalous precipitation is regressed on the positive and negative phase of the concurrent ENSO SST index covering its SST main action center in the central-eastern equatorial Pacific (90°-180°W, 5°S-5°N). Other ENSO quantities and associated feedback terms are also calculated in a similar manner. Compared to a composite analysis, such a regression approach has the advantages of avoiding a subjective choice of the ENSO event threshold and of cleanly separating the contribution of SST-precipitation sensitivity and ENSO SST variability to total ENSO precipitation changes. This regression approach is more representative of the strong ENSO variability[42]. In particular, the symmetric and asymmetric parts of the regressed strong El Niño and La Niña DJF SST anomalies in the PD simulation of the CESM1.2 model are quite similar to the two leading Empirical Orthogonal Function (EOF) modes of the concurrent tropical Pacific SST anomalies, which together account for about 85% of the total variability (Supplementary Fig. 1).

In the CESM1.2 model, the DJF seasonal climatology and anomalies are defined using the full period for the PD simulation, while the 28-member ensemble mean and corresponding deviations in each member are computed for the CO_2 ramp-up and ramp-down experiments. Given that only one realization is available for each CMIP6 model, the DJF climatology and anomalies in each model are defined in each 31-year window of three selected time slices based on their respective GMST evolution. The two-tailed Student's *t*-test is used to determine the statistical significance level of the 28-member ensemble-averaged climate change signals relative to the PD control simulation. For the CESM1.2 present-day simulation, a 900-year simulation length with a 31-year moving window corresponds to an effective sample size of 29, which is comparable to the ensemble member size of 28 in the CO_2 ramp-up and ramp-down experiments.

Vertical mode decomposition

Shallow and deep convection types in the CESM1.2 model are separated based on their vertical motion profiles[25,41]. In a practical sense, the two leading statistical vertical structures (Ω_1 and Ω_2) are first derived by applying an EOF analysis to the 12-month seasonal climatological vertical pressure velocity (ω) between 1000 hPa and 100 hPa and over the tropical oceans from 20°S to 20°N. Since the EOF results are arbitrary as to sign, the derived Ω_1 and Ω_2 have to be corrected, if necessary, to have a low-level

upward motion (i.e., $\omega < 0$; Supplementary Fig. 4a) for subsequent combinations. Before the EOF analysis, the ω field is also linearly interpolated in the vertical direction with an equal level spacing of 50 hPa to avoid weighting problems associated with the uneven vertical grid spacing coming from the raw model output. The vertical motion structures of shallow (Ω_s) and deep (Ω_d) convection can then be obtained by linearly combining Ω_1 and Ω_2:

$$\begin{cases} \Omega_s = -\Omega_1 + r\Omega_2 \\ \Omega_d = r\Omega_1 + \Omega_2 \end{cases} \quad (1)$$

The assumptions of (i) orthogonality between two constructed vertical modes and (ii) zero near-surface convergence for the shallow mode determine the combination ratio parameter r:

$$r = -\frac{\Omega_2(1000\,hPa) - \Omega_2(950\,hPa)}{\Omega_1(1000\,hPa) - \Omega_1(950\,hPa)} \quad (2)$$

Once we derive the vertical structures of shallow and deep convection, the associated anomalous vertical pressure velocity can be easily obtained by applying vector projection and reconstruction operations to the three-dimensional vertical pressure velocity field. We adopt fixed shallow and deep convection vertical structures (i.e., Ω_s and Ω_d) from the PD simulation throughout our analysis, as they show less change at different stages of the ramp-up and ramp-down conditions (Supplementary Fig. 4). In the PD simulation, Ω_1 and Ω_2 explain 89% and 8% of the total variance of climatological vertical motion, respectively. With a combination ratio parameter $r = -1.64$, the shallow and deep convection structures account for 30% and 67% of the total variance of the climatological vertical motions over the tropical oceans, respectively.

Moisture budget analysis

The anomalous column-integrated moisture budget equation[65] with neglected time tendency term is used to quantify the moisture feedback processes that drive the ENSO precipitation anomaly:

$$P' = -\langle\omega' \cdot \bar{q}_p\rangle - \langle\vec{V}_2' \cdot \nabla_2 \bar{q}\rangle - \langle\bar{\vec{V}}_3 \cdot \nabla_3 q'\rangle - \langle\vec{V}_3' \cdot \nabla_3 q'\rangle + E' \quad (3)$$

and its future changes:

$$\begin{aligned} \Delta P' = &-\langle\Delta\omega_s' \cdot (\bar{q}_p)^{PD}\rangle - \langle\Delta\omega_d' \cdot (\bar{q}_p)^{PD}\rangle - \langle(\omega')^{PD} \cdot \Delta\bar{q}_p\rangle \\ &- \langle\Delta\omega' \cdot \Delta\bar{q}_p\rangle - \Delta\left(\langle\vec{V}_2' \cdot \nabla_2 \bar{q}\rangle\right) - \Delta\left(\langle\bar{\vec{V}}_3 \cdot \nabla_3 q'\rangle\right) \\ &- \Delta\left(\langle\vec{V}_3' \cdot \nabla_3 q'\rangle\right) + \Delta E' \end{aligned} \quad (4)$$

In the above two equations, P and E represent the precipitation and surface upward evaporation flux, while q, ω, $\vec{V}_2 = (u, v)$, and $\vec{V}_3 = (u, v, \omega)$ are the specific humidity, vertical pressure velocity, horizontal, and three-dimensional atmospheric circulation at the pressure level, respectively. ω_s and ω_d are the vertical pressure velocities associated with shallow and deep convection. The Δ represents the future change in a physical quantity relative to that in the baseline simulation and is calculated as the difference between the ensemble mean of the CO_2 ramp-up and ramp-down experiments relative to the long-term mean in the PD simulation. Variables with overbars and primes represent the background mean state and anomalies, while those with a *PD* superscript in Eq. 4 indicate that the quantity is from the PD simulation. The angle bracket is a vertical integration operator that integrates a physical quantity (A) at the pressure level from the surface to the top of the atmosphere:

$$\langle A\rangle = \frac{1}{g}\int_{P_{top}}^{P_{sfc}} A(p) \cdot dp \quad (5)$$

where $g = 9.81\ m\ s^{-2}$ is the gravitational acceleration, $P_{top} = 100$ hPa, and $P_{sfc} = 1000$ hPa.

MSE budget analysis and heat flux decomposition

The MSE equation, derived by combining the vertically integrated thermodynamic and moisture equations, can avoid large canceling terms that occur in the individual moisture and temperature equations[66], and is often used to diagnose feedback processes related to the vertical motion of deep convection. The MSE equation with the neglected time tendency term is reorganized as follows:

$$\begin{aligned} \langle\omega_d' \cdot \bar{h}_p\rangle = &-\langle\omega_s' \cdot \bar{h}_p\rangle - \langle\vec{V}_2' \cdot \nabla_2 \bar{k}\rangle - \langle\bar{\vec{V}}_2 \cdot \nabla_2 k'\rangle - \langle\vec{V}_2' \cdot \nabla_2 k'\rangle \\ &- \langle\bar{\omega} \cdot h_p'\rangle - \langle\omega' \cdot h_p'\rangle + F_{net}' \end{aligned} \quad (6)$$

On this basis, the future changes in ENSO-induced deep convection can be achieved:

$$\begin{aligned} \langle\Delta\omega_d' \cdot \left(\bar{h}_p\right)^{PD}\rangle = &-\langle\Delta\omega_s' \cdot \left(\bar{h}_p\right)^{PD}\rangle - \langle(\omega')^{PD} \cdot \Delta\bar{h}_p\rangle - \langle\Delta\omega' \cdot \Delta\bar{h}_p\rangle \\ &- \Delta\left(\langle\vec{V}_2' \cdot \nabla_2 \bar{k}\rangle\right) - \Delta\left(\langle\bar{\vec{V}}_2 \cdot \nabla_2 k'\rangle\right) - \Delta\left(\langle\vec{V}_2' \cdot \nabla_2 k'\rangle\right) \\ &- \Delta\left(\langle\bar{\omega} \cdot h_p'\rangle\right) - \Delta\left(\langle\omega' \cdot h_p'\rangle\right) + \Delta F_{net}' \end{aligned} \quad (7)$$

The symbols in Eq. 6 and Eq. 7 are mostly the same as in Eq. 3 and Eq. 4. The MSE is $h = C_p T + L_v q + gz$, the moist enthalpy is $k = C_p T + L_v q$, where T, q, and z are the air temperature, specific humidity, and geopotential height at the pressure level. $C_p = 1005.7\ J\ kg^{-1}\ K^{-1}$ and $L_v = 2.5104 \times 10^6\ J\ kg^{-1}$ are the specific heat at constant pressure and the latent heat of vaporization, respectively.

F_{net} is the net heat flux entering the air column and is evaluated as the sum of the net downward heat flux at the top of the atmosphere and the net upward heat flux at the sea surface. The longwave flux is further separated into cloud-related and clear-sky components:

$$\Delta F_{net}' = \Delta Q_{sw}' + \Delta Q_{lw-cld}' + \Delta Q_{lw-clr}' + \Delta Q_{sh}' + \Delta Q_{lh}' \quad (8)$$

Here, Q_{sw}, Q_{lw}, Q_{sh}, and Q_{lh} denote the net shortwave flux, net longwave flux, net sensible heat flux, and net latent heat flux absorbed by the atmosphere, with the subscripts "cld" and "clr" denoting the cloud-related and clear-sky components of the net longwave flux, respectively.

Latent heat flux decomposition

The surface latent heat flux (Q_{lh}) is influenced by multiple processes[51,52]. Specifically, according to the bulk formula equation:

$$Q_{lh} = L_v \rho_a C_E W\left(1 - RHe^{\alpha S}\right) q_s \quad (9)$$

it can be linearly decomposed into the effects of Newtonian cooling, wind speed, stability, and relative humidity to disentangle the key background states that control the sensitivity of the anomalous latent heat flux to environmental perturbations:

$$\begin{aligned} \left(Q_{lh}^{SST}\right)' &= \frac{\partial Q_{lh}}{\partial SST} SST' = \alpha\overline{Q_{lh}} SST' \\ \left(Q_{lh}^{W}\right)' &= \frac{\partial Q_{lh}}{\partial W} W' = \frac{\overline{Q_{lh}}}{\overline{W}} W' \\ \left(Q_{lh}^{S}\right)' &= \frac{\partial Q_{lh}}{\partial S} S' = \frac{-\alpha\overline{RHQ_{lh}}e^{\alpha\bar{S}}}{\left(1 - \overline{RH}e^{\alpha\bar{S}}\right)} S' \\ \left(Q_{lh}^{RH}\right)' &= \frac{\partial Q_{lh}}{\partial RH} RH' = \frac{-\alpha\overline{Q_{lh}}e^{\alpha\bar{S}}}{\left(1 - \overline{RH}e^{\alpha\bar{S}}\right)} RH' \end{aligned} \quad (10)$$

In Eq. 9 and Eq. 10, $\rho_a = 1.225\ \mathrm{kg\ m^{-3}}$ is the surface air density, $C_E = 1.1 \times 10^{-3}$ is the dimensionless transfer coefficient, W is the surface wind speed, RH is the relative humidity, α is a constant value of about $0.06\ \mathrm{K^{-1}}$ in the tropics, $S = T_a$ - SST is the surface stability parameter measured as the temperature contrast between the 2 m air and the underlying SST, and q_s is the sea surface saturation specific humidity as a function of SST.

Atmospheric boundary layer model

Shallow convective precipitation is strongly influenced by the underlying SST structure, which shapes the horizontal distribution of boundary layer temperature and moisture, pressure gradients, and convergence. Following previous studies[17,23,41,49], we adopted a simple atmospheric mixed-layer model to disentangle the contribution of boundary layer wind anomalies contributed by the ENSO SST and other free tropospheric processes. This model is built on the horizontal boundary layer momentum balance of pressure gradients, Coriolis effect, linear fractional drag, and downward momentum mixing from the free troposphere. The analytical solution of the horizontal boundary layer winds, including the momentum mixing and surface pressure terms, is given by:

$$\begin{aligned} U &= \frac{U_{850}\varepsilon_i\varepsilon_e + V_{850}f\varepsilon_e}{\varepsilon_i^2 + f^2} - \frac{\left(f\frac{\partial P_s}{\partial y} + \varepsilon_i\frac{\partial P_s}{\partial x}\right)}{\rho_0(\varepsilon_i^2 + f^2)} \\ V &= \frac{V_{850}\varepsilon_i\varepsilon_e - U_{850}f\varepsilon_e}{\varepsilon_i^2 + f^2} + \frac{\left(f\frac{\partial P_s}{\partial x} - \varepsilon_i\frac{\partial P_s}{\partial y}\right)}{\rho_0(\varepsilon_i^2 + f^2)} \end{aligned} \tag{11}$$

where U_{850}, V_{850}, P_s, f, $\rho_0 = 1.225\ \mathrm{kg\ m^{-3}}$, $\varepsilon_e = 2.0 \times 10^{-5}\ \mathrm{s^{-1}}$, and $\varepsilon_i = 3.5 \times 10^{-5}\ \mathrm{s^{-1}}$ are 850 hPa zonal wind, 850 hPa meridional wind, surface pressure, Coriolis parameter, planetary boundary air density, and two empirical parameters related to friction and entrainment mixing at the top of the boundary layer, respectively.

The surface pressure (P_S) is contributed by the air mass in the boundary layer and the free troposphere above. The free tropospheric component (P_i) is the local pressure at a nominal boundary layer top located at the mean height of the 850-hPa pressure surface $\bar{z}_{850}$. Using the hydrostatic relation and the ideal gas law[41], the P_i can be calculated as follows:

$$P_i = \frac{P_S}{e^{\int_0^{\bar{z}_{850}} \frac{g}{R_d T_v} dz}} \tag{12}$$

where $R_d = 287.04\ \mathrm{J\ kg^{-1}\ K^{-1}}$ is the gas constant for dry air, T_v is the virtual temperature. The denominator is the exponential of the boundary layer integrated virtual temperature inverse up to some constants. In practice, the boundary layer vertical integration operator is evaluated in the pressure coordinate system by approximating the upper boundary at 850 hPa and using the hydrostatic relation[41]. On this basis, the boundary layer component (P_{BL}) of the surface pressure is estimated as a residual with $P_{BL} = P_s - P_i$. Replacing the "P_s" in Eq. 11 with "P_i" and "P_{BL}", and neglecting the mixing term associated with U_{850}, V_{850}, we can estimate the surface wind and convergence contributed by the free tropospheric and boundary layer pressures.

Ocean mixed layer heat budget

Following our previous studies[30,31], we used a partial flux form of the ocean mixed layer heat budget[67] to understand the physical processes of ENSO SST structure changes:

$$\begin{aligned} \frac{\partial T}{\partial t} = {} & \frac{Q}{\rho C_p H_{mld}} - \left(\frac{\partial(\bar{u}T)}{\partial x} + \frac{\partial(\bar{v}T)}{\partial y}\right) + \frac{\bar{W}T_{sub}}{H_{mld}} \\ & - \left(u\frac{\partial \bar{T}}{\partial x} + v\frac{\partial \bar{T}}{\partial y} + w\frac{\partial \bar{T}}{\partial z}\right) - \left(u\frac{\partial T}{\partial x} + v\frac{\partial T}{\partial y} + w\frac{\partial T}{\partial z}\right) \end{aligned} \tag{13}$$

The variables T, u, v, and w denote mixed layer ocean temperature and zonal, meridional, and vertical ocean current velocities, respectively. Variables with and without an over-bar represent background mean states and anomalies, respectively. T_{sub} and W are the ocean temperature anomalies and the background vertical current velocity at the base of the mixed layer. The mixed layer depth is taken as a constant depth of 50 m ($H_{mld} = 50$ m), while $\rho = 1026\ \mathrm{kg\ m^{-3}}$ and $C_p = 3996\ \mathrm{J\ kg^{-1}\ K^{-1}}$ are seawater density and heat capacity. Q denotes sea surface net heat flux anomalies into the ocean. The six grouped terms on the right-hand side are thermal damping by net heat flux (Q_{net}), dynamical damping by horizontal mean circulation (DD), thermocline feedback (TH), advective feedback (ADV), and nonlinear dynamical heating (NDH), respectively. Advective feedback includes zonal advective feedback, meridional advective feedback, and Ekman feedback.

Data availability

The ERA5 data is available at https://www.ecmwf.int/en/forecasts/dataset/ecmwf-reanalysis-v5. The CESM1.2 model data used in this study is available at https://figshare.com/s/13946511eb876445f10e. The CMIP6 model data is available at https://esgf-metagrid.cloud.dkrz.de/search/cmip6-dkrz/.

Code availability

The model code for CESM1.2 is available at https://www2.cesm.ucar.edu/models/cesm1.2/. Figure codes are available upon request from the first and corresponding authors.

Received: 8 June 2024; Accepted: 6 December 2024;
Published online: 19 December 2024

References

1. Anttila-Hughes, J. K., Jina, A. S. & McCord, G. C. ENSO impacts child undernutrition in the global tropics. *Nat. Commun.* **12**, 5785 (2021).
2. Callahan, C. W. & Mankin, J. S. Persistent effect of El Niño on global economic growth. *Science* **380**, 1064–1069 (2023).
3. Liu, Y., Cai, W., Lin, X., Li, Z. & Zhang, Y. Nonlinear El Niño impacts on the global economy under climate change. *Nat. Commun.* **14**, 5887 (2023).
4. McPhaden, M. J., Zebiak, S. E. & Glantz, M. H. ENSO as an integrating concept in earth science. *Science* **314**, 1740–1745 (2006).
5. Neelin, J. D. et al. ENSO theory. *J. Geophys Res Oceans* **103**, 14261–14290 (1998).
6. Taschetto, A. S. et al. ENSO Atmospheric teleconnections. in El Niño southern oscillation in a changing climate. 309–335. https://doi.org/10.1002/9781119548164.ch14 (2020).
7. Beverley, J. D., Newman, M. & Hoell, A. Rapid development of systematic ENSO-related seasonal forecast errors. *Geophys. Res. Lett.* **50**, e2022GL102249 (2023).
8. Cai, W. et al. Changing El Niño–Southern Oscillation in a warming climate. *Nat. Rev. Earth Environ.* **2**, 628–644 (2021).
9. L'Heureux, M. L. et al. ENSO prediction. in *El Niño Southern Oscillation in a Changing Climate.* 227–246. https://doi.org/10.1002/9781119548164.ch10 (2020).
10. Bonfils, C. J. W. et al. Relative contributions of mean-state shifts and ENSO-driven variability to precipitation changes in a warming climate. *J. Clim.* **28**, 9997–10013 (2015).
11. Cai, W. et al. Increasing frequency of extreme El Niño events due to greenhouse warming. *Nat. Clim. Chang.* **4**, 111–116 (2014).
12. Huang, P. & Xie, S.-P. Mechanisms of change in ENSO-induced tropical Pacific rainfall variability in a warming climate. *Nat. Geosci.* **8**, 922–926 (2015).
13. Huang, P. Time-varying response of ENSO-induced tropical pacific rainfall to global warming in CMIP5 models. Part I: Multimodel ensemble results. *J. Clim.* **29**, 5763–5778 (2016).
14. Huang, P. Time-Varying Response of ENSO-Induced Tropical Pacific Rainfall to Global Warming in CMIP5 Models. Part II: Intermodel Uncertainty. *J. Clim.* **30**, 595–608 (2017).

15. Power, S., Delage, F., Chung, C., Kociuba, G. & Keay, K. Robust twenty-first-century projections of El Niño and related precipitation variability. *Nature* **502**, 541–545 (2013).
16. Power, S. B., Delage, F. P. D., Chung, C. T. Y., Ye, H. & Murphy, B. F. Humans have already increased the risk of major disruptions to Pacific rainfall. *Nat. Commun.* **8**, 14368 (2017).
17. Yan, Z. et al. Eastward shift and extension of ENSO-induced tropical precipitation anomalies under global warming. *Sci. Adv.* **6**, eaax4177 (2020).
18. Yun, K.-S. et al. Increasing ENSO–rainfall variability due to changes in future tropical temperature–rainfall relationship. *Commun. Earth Environ.* **2**, 43 (2021).
19. Bayr, T., Dommenget, D., Martin, T. & Power, S. B. The eastward shift of the Walker Circulation in response to global warming and its relationship to ENSO variability. *Clim. Dyn.* **43**, 2747–2763 (2014).
20. Held, I. M. & Soden, B. J. Robust responses of the hydrological cycle to global warming. *J. Clim.* **19**, 5686–5699 (2006).
21. Chen, L., Li, T., Yu, Y. & Behera, S. K. A possible explanation for the divergent projection of ENSO amplitude change under global warming. *Clim. Dyn.* **49**, 3799–3811 (2017).
22. Hayashi, M., Jin, F.-F. & Stuecker, M. F. Dynamics for El Niño-La Niña asymmetry constrain equatorial-Pacific warming pattern. *Nat. Commun.* **11**, 4230 (2020).
23. Back, L. E. & Bretherton, C. S. On the relationship between SST gradients, boundary layer winds, and convergence over the tropical oceans. *J. Clim.* **22**, 4182–4196 (2009).
24. Bui, H. X., Yu, J.-Y. & Chou, C. Impacts of vertical structure of large-scale vertical motion in tropical climate: moist static energy framework. *J. Atmos. Sci.* **73**, 4427–4437 (2016).
25. Back, L. E. & Bretherton, C. S. A simple model of climatological rainfall and vertical motion patterns over the tropical oceans. *J. Clim.* **22**, 6477–6497 (2009).
26. Neelin, J. D. & Held, I. M. Modeling tropical convergence based on the moist static energy budget. *Mon. Weather Rev.* **115**, 3–12 (1987).
27. Sun, N. et al. Amplified tropical Pacific rainfall variability related to background SST warming. *Clim. Dyn.* **54**, 2387–2402 (2020).
28. Sobel, A. H. Simple models of ensemble-averaged tropical precipitation and surface wind, given the sea surface temperature. in *The Global Circulation of the Atmosphere* 219–251. https://doi.org/10.1515/9780691236919-010 (Princeton University Press, 2008).
29. Yan, Z., Wu, B., Li, T. & Tan, G. Mechanisms determining diversity of ENSO-driven equatorial precipitation anomalies. *J. Clim.* **35**, 923–939 (2022).
30. Liu, C. et al. Hysteresis of the El Niño–southern oscillation to CO_2 forcing. *Sci. Adv.* **9**, eadh8442 (2023).
31. Liu, C. et al. ENSO skewness hysteresis and associated changes in strong El Niño under a CO_2 removal scenario. *NPJ Clim. Atmos. Sci.* **6**, 117 (2023).
32. Pathirana, G. et al. Increase in convective extreme El Niño events in a CO_2 removal scenario. *Sci. Adv.* **9**, eadh2412 (2023).
33. Kug, J.-S. et al. Hysteresis of the intertropical convergence zone to CO_2 forcing. *Nat. Clim. Chang* **12**, 47–53 (2021).
34. An, S.-I. et al. Asymmetric ENSO teleconnections in a symmetric CO_2 concentration pathway. *Environ. Res. Lett.* https://doi.org/10.1088/1748-9326/ad7b5c (2024).
35. Hurrell, J. W. et al. The Community Earth System Model: a framework for collaborative research. *Bull. Am. Meteorol. Soc.* **94**, 1339–1360 (2013).
36. DiNezio, P. N., Deser, C., Okumura, Y. & Karspeck, A. Predictability of 2-year La Niña events in a coupled general circulation model. *Clim. Dyn.* **49**, 4237–4261 (2017).
37. Wu, X., Okumura, Y. M. & DiNezio, P. N. What controls the duration of El Niño and La Niña events? *J. Clim.* **32**, 5941–5965 (2019).
38. Kim, J.-W. & Yu, J.-Y. Single- and multi-year ENSO events controlled by pantropical climate interactions. *NPJ Clim. Atmos. Sci.* **5**, 88 (2022).
39. Thirumalai, K. et al. Future increase in extreme El Niño supported by past glacial changes. *Nature* **634**, 374–380 (2024).
40. Deng, J. & Dai, A. Arctic sea ice–air interactions weaken El Niño–Southern oscillation. *Sci. Adv.* **10**, eadk3990 (2024).
41. Duffy, M. L., O'Gorman, P. A. & Back, L. E. Importance of Laplacian of low-level warming for the response of precipitation to climate change over tropical oceans. *J. Clim.* **33**, 4403–4417 (2020).
42. Frankignoul, C. & Kwon, Y. On the statistical estimation of asymmetrical relationship between two climate variables. *Geophys. Res. Lett.* **49**, e2022GL100777 (2022).
43. Bellenger, H., Guilyardi, E., Leloup, J., Lengaigne, M. & Vialard, J. ENSO representation in climate models: from CMIP3 to CMIP5. *Clim. Dyn.* **42**, 1999–2018 (2014).
44. Wu, X., Okumura, Y. M., DiNezio, P. N., Yeager, S. G. & Deser, C. The Equatorial Pacific Cold Tongue Bias in CESM1 and Its Influence on ENSO Forecasts. *J. Clim.* **35**, 3261–3277 (2022).
45. Bayr, T., Lübbecke, J. F., Vialard, J. & Latif, M. Equatorial Pacific Cold Tongue Bias degrades simulation of ENSO Asymmetry due to underestimation of strong Eastern Pacific El Niños. *J. Clim.* https://doi.org/10.1175/JCLI-D-24-0071.1 (2024).
46. Wittenberg, A. T. Are historical records sufficient to constrain ENSO simulations? *Geophys. Res. Lett.* **36**, L12702 (2009).
47. An, S. et al. Global cooling hiatus driven by an AMOC overshoot in a carbon dioxide removal scenario. *Earths Future* **9**, e2021EF002165 (2021).
48. Yano, J.-I. & Plant, R. Interactions between shallow and deep convection under a finite departure from convective quasi equilibrium. *J. Atmos. Sci.* **69**, 3463–3470 (2012).
49. Stevens, B., Duan, J., McWilliams, J. C., Münnich, M. & Neelin, J. D. Entrainment, Rayleigh friction, and boundary layer winds over the tropical pacific. *J. Clim.* **15**, 30–44 (2002).
50. Koll, D. D. B., Jeevanjee, N. & Lutsko, N. J. An analytic model for the clear-sky longwave feedback. *J. Atmos. Sci.* **80**, 1923–1951 (2023).
51. Xie, S.-P. et al. Global warming pattern formation: sea surface temperature and rainfall. *J. Clim.* **23**, 966–986 (2010).
52. He, C. et al. A North Atlantic warming hole without ocean circulation. *Geophys. Res. Lett.* **49**, e2022GL100420 (2022).
53. Zhou, S., Huang, P., Xie, S.-P., Huang, G. & Wang, L. Varying contributions of fast and slow responses cause asymmetric tropical rainfall change between CO_2 ramp-up and ramp-down. *Sci. Bull.* **67**, 1702–1711 (2022).
54. Oh, J.-H. et al. Emergent climate change patterns originating from deep ocean warming in climate mitigation scenarios. *Nat. Clim. Chang.* **14**, 260–266 (2024).
55. Peng, Q. et al. Surface warming–induced global acceleration of upper ocean currents. *Sci. Adv.* **8**, eabj8394 (2022).
56. Hu, S. & Fedorov, A. V. Cross-equatorial winds control El Niño diversity and change. *Nat. Clim. Chang.* **8**, 798–802 (2018).
57. Pausata, F. S. R., Zanchettin, D., Karamperidou, C., Caballero, R. & Battisti, D. S. ITCZ shift and extratropical teleconnections drive ENSO response to volcanic eruptions. *Sci. Adv.* **6**, eaaz5006 (2020).
58. Pontes, G. M. et al. Mid-Pliocene El Niño/Southern Oscillation suppressed by Pacific intertropical convergence zone shift. *Nat. Geosci.* **15**, 726–734 (2022).
59. Eyring, V. et al. Overview of the Coupled Model Intercomparison Project Phase 6 (CMIP6) experimental design and organization. *Geosci. Model Dev.* **9**, 1937–1958 (2016).
60. Keller, D. P. et al. The Carbon Dioxide Removal Model Intercomparison Project (CDRMIP): rationale and experimental protocol for CMIP6. *Geosci. Model Dev.* **11**, 1133–1160 (2018).
61. DiNezio, P. N. et al. A 2 year forecast for a 60–80% chance of La Niña in 2017–2018. *Geophys. Res. Lett.* **44**, 11624–11635 (2017).

62. Okumura, Y. M., Sun, T. & Wu, X. Asymmetric modulation of El Niño and La Niña and the linkage to tropical pacific decadal variability. *J. Clim.* **30**, 4705–4733 (2017).
63. Zhang, T., Shao, X. & Li, S. Impacts of atmospheric processes on ENSO asymmetry: a comparison between CESM1 and CCSM4. *J. Clim.* **30**, 9743–9762 (2017).
64. Hersbach, H. et al. The ERA5 global reanalysis. *Q. J. R. Meteorol. Soc.* **146**, 1999–2049 (2020).
65. Adames, Á. F. & Ming, Y. Moisture and moist static energy budgets of South Asian monsoon low pressure systems in GFDL AM4.0. *J. Atmos. Sci.* **75**, 2107–2123 (2018).
66. Neelin, J. D. Moist dynamics of tropical convection zones in monsoons, teleconnections, and global warming. in *The Global Circulation of the Atmosphere* 267–301 https://doi.org/10.1515/9780691236919-012 (Princeton University Press, 2008).
67. An, S.-I., Jin, F.-F. & Kang, I.-S. The role of zonal advection feedback in phase transition and growth of ENSO in the Cane-Zebiak model. *J. Meteorol. Soc. Jpn. Ser. II* **77**, 1151–1160 (1999).

Acknowledgements

We would like to thank Dr. Jongsoo Shin for his time and effort in performing the large ensemble CO_2 ramp-up and ramp-down simulations using the CESM1.2 model. This work was supported by National Research Foundation of Korea (NRF) grants funded by the Korean government (MSIT) (NRF-2018R1A5A1024958). S.I.A. was supported by the Yonsei Fellowship, funded by Lee Youn Jae. Model simulation and data transfer were supported by the National Supercomputing Center with supercomputing resources including technical support (KSC-2019-CHA-0005), the National Center for Meteorological Supercomputer of the Korea Meteorological Administration, and the Korea Research Environment Open NETwork (KREONET), respectively.

Author contributions

C.L. and S.I.A. conceived the idea. C.L. and Z.X.Y. designed the study and the methodology. C.L. performed the analysis, prepared all figures, and drafted the first version of the manuscript. S.I.A. directed the research and supervised the project. C.L., S.I.A., Z.X.Y., S.K.K., and S.P. contributed to the interpretation of the results and the improvement of the manuscript.

Competing interests

The authors declare no competing interests.

Additional information

Supplementary information The online version contains supplementary material available at https://doi.org/10.1038/s43247-024-01958-8.

Correspondence and requests for materials should be addressed to Soon-Il An.

Peer review information *Communications Earth & Environment* thanks the anonymous reviewers for their contribution to the peer review of this work. Primary Handling Editors: José Luis Iriarte Machuca and Alireza Bahadori. A peer review file is available

Reprints and permissions information is available at http://www.nature.com/reprints

Publisher's note Springer Nature remains neutral with regard to jurisdictional claims in published maps and institutional affiliations.

Open Access This article is licensed under a Creative Commons Attribution-NonCommercial-NoDerivatives 4.0 International License, which permits any non-commercial use, sharing, distribution and reproduction in any medium or format, as long as you give appropriate credit to the original author(s) and the source, provide a link to the Creative Commons licence, and indicate if you modified the licensed material. You do not have permission under this licence to share adapted material derived from this article or parts of it. The images or other third party material in this article are included in the article's Creative Commons licence, unless indicated otherwise in a credit line to the material. If material is not included in the article's Creative Commons licence and your intended use is not permitted by statutory regulation or exceeds the permitted use, you will need to obtain permission directly from the copyright holder. To view a copy of this licence, visit http://creativecommons.org/licenses/by-nc-nd/4.0/.

© The Author(s) 2024